

## RESEARCH ARTICLE

# A case study of temperature tendency mechanisms operating over northern Africa during and following midlatitude winter troughs

Neil Ward<sup>1</sup>  | Andreas H. Fink<sup>2</sup>  | Richard J. Keane<sup>1,3</sup> | Douglas J. Parker<sup>1,4,5</sup> 

<sup>1</sup>School of Earth and Environment,  
University of Leeds, Leeds,  
United Kingdom

<sup>2</sup>Institute for Meteorology and Climate  
Research, Karlsruhe Institute for  
Technology, Karlsruhe, Germany

<sup>3</sup>Met Office, Exeter, United Kingdom

<sup>4</sup>National Centre for Atmospheric Science  
(NCAS), University of Leeds,  
United Kingdom

<sup>5</sup>NORCE Norwegian Research Centre AS,  
Bjerknes Center for Climate Research,  
Bergen, Norway

## Correspondence

Douglas J. Parker, School of Earth and  
Environment, University of Leeds, Leeds,  
United Kingdom.

Email: [d.j.parker@leeds.ac.uk](mailto:d.j.parker@leeds.ac.uk)

## Funding information

UK Research and Innovation as part of the  
Global Challenges Research Fund, African  
SWIFT programme, NE/P021077/1;  
Deutsche Forschungsgemeinschaft,  
Grant/Award Number: SFB/TRR 165;  
CEMAC (University of Leeds);  
AMMA-2050; IMPALA, Grant/Award  
Numbers: NERC/DFID NE/M017176/1,  
NERC/DFID NE/M020126/1

## Abstract

We investigate temperature tendency mechanisms operating over northern Africa following midlatitude upper-level winter troughs. A case study sequence reveals how Iberia and Central Mediterranean troughs perturb the prevailing cold advection of the Harmattan winds, leading to a several-day warming event over northeastern Africa, especially marked over the eastern Sahel (ESL). Data used includes a reanalysis product that attributes three-hour temperature tendency to specific mechanisms. Focused over Days 3–5 (Day 0 is the strong Iberia trough), ESL experiences strong anomalous low-level warming due to dynamics, attributable to anomalous meridional advection, with partial damping by turbulence, leaving a net low-level tendency of about +1°C/day. However, these tendency features are confined to the lowest layers; by 700 hPa, they are absent. Net tendency behaves differently, and remains positive up to near 650 hPa, where the boundary layer anomalously rises to in the afternoon, allowing turbulence to share some of the anomalous warm advection to these levels. In this winter case study, there is no evidence of any other substantial forcing or feedback (e.g., from atmospheric moisture radiation, surface latent heating, surface solar radiation), therefore we propose that over ESL, the land-surface—boundary-layer system adjusts towards a new equilibrium, driven by the several-day reduced cold advection from near-surface to about 850 hPa. The trough sequence induces a continental-scale cold front, that approaches ESL with distinct advection properties; however, on average, extended warming in ESL events is attributed to advection by the climatological meridional wind operating on the anomalous temperature gradient. During build-up (e.g. Day 0), anomalous descent over ESL contributes a modest adiabatic compression warming tendency at low levels. In contrast, averaged over Days 3–5, there is modest anomalous ascent, one aspect of the boundary-layer characteristics during the reduced cold advection that are explored. Generalization of highlighted processes now requires more cases.

## KEYWORDS

advection, Africa, dynamics, Sahel, temperature, tendency, weather, winter troughs

This is an open access article under the terms of the [Creative Commons Attribution](https://creativecommons.org/licenses/by/4.0/) License, which permits use, distribution and reproduction in any medium, provided the original work is properly cited.

© 2025 Crown copyright and The Author(s). *Quarterly Journal of the Royal Meteorological Society* published by John Wiley & Sons Ltd on behalf of Royal Meteorological Society. This article is published with the permission of the Controller of HMSO and the King's Printer for Scotland.

# 1 | INTRODUCTION

There is a clear need to better understand the causes of the observed low-level synoptic timescale temperature variability generally within the climate system, and in particular, in vulnerable locations like northern Africa. Such advances will enable better characterization of heat (e.g., Fontaine et al., 2013; Hu et al., 2019; Ragatoa et al., 2024) and cold waves (Vizy & Cook, 2014) to improve numerical and statistical weather forecasts (e.g., Rasheeda Satheesh et al., 2025) and to improve incorporation of the features in models for climate projection (e.g., Cook & Vizy, 2015, 2024).

In this study, we focus on a particular type of temperature variation in winter over northern Africa that is known to be associated with, and persist after, the presence of midlatitude winter troughs to the north (Knippertz & Fink, 2008; Taylor et al., 2018, hereafter, T18; Ward et al., 2023, hereafter, W23). We consider this a useful entry point to the causes of large temperature variation over several days in this region at this time of year. In addition, the analysis contributes further understanding to the operation of this mode of winter weather variation, that also includes equatorial rainfall to the south, and taken together, forms an important regional seasonal climate fluctuation (Knippertz & Fink, 2008; Ward et al., 2021, hereafter, W21).

A particular emphasis is the eastern Sahel (ESL, approximately 9–15° N, 24–34° E), which is very dry with desiccated soils at this time of year, and where the temperature fluctuation following upper-level troughs is especially strong and persistent at these low latitudes. While the warmest temperatures in this region are climatologically found a little later in the annual cycle in spring, the temperature variability in winter is still relevant to human activity, both anomalies of cold and heat, and especially in late winter, temperatures can climb to heat-stress levels. For example, in early February 2018, daytime maximum temperatures reached over 40°C at Khartoum, while in March 2024 several consecutive days of maximum temperatures above 40°C were experienced across ESL with significant impacts (NASA, 2024). Furthermore, winter warm spells in this region are considered physical drivers of unusually heavy rainfall events to the south over northern Congo (T18; W21), so better representation of ESL temperature in models can also be expected to lead to improved rainfall in weather forecasts and climate projections over the Congo (Andrews et al., 2024; Cook et al., 2020; Hart et al., 2019).

This paper analyses a case study event (in February 2018) that follows the sequence identified in W21, with a strong upper-level trough first over Iberia, that transitions over 2–3 days to the Central Mediterranean, leading to large-scale spatially-evolving low-level warming across

northeastern Africa (approximately 5–35° N, 5–35° E), particularly strong over the subsequent few days extending deeply into the tropics and especially ESL. The research addresses the physical and dynamical processes that give rise to the temperature tendencies across northern Africa during these days. In other words, we focus on the mechanism of warming (and cooling) once the large-scale circulation anomaly is in place.

In addition to ERA5 (Hersbach et al., 2020), the paper draws on an enhanced ECMWF product for the recent period 2018–2020 (referred to as Year of Polar Prediction, YOPP, Bauer et al., 2020), in which each 3-hour temperature tendency at each grid location is broken out into six process components, the most useful here being tendency due to dynamics, turbulent diffusion and radiation. Each of these could potentially have a strong role to play. In some northern Africa spring heat waves, a key role for radiation is proposed due to increased moisture leading to a night-time water vapour greenhouse effect (e.g., Largeron et al., 2020; Oueslati et al., 2017), although cases in moist monsoon flow are in contrast to the arid case here. In a composite analysis of heatwaves in central northern Africa (7–15° N, 15–30° E) conducted across all seasons, Hu et al. (2019) argued for an important role for an aspect of dynamical process, namely horizontal low-level advection, with the full wind (mainly northerly) operating on the anomalous meridional temperature gradient. While their analysis made that conclusion through subjective visualization of wind and temperature composite maps, here we make a more objective calculation. In fact, the YOPP dynamics term is contributed to by both horizontal advection, and by the impact on temperature tendency by vertical motion (compression). We therefore separate the dynamics term into those two components. In addition, using ERA5 (1982–2020), we make a separate cross-check validation of the horizontal advection at 850 hPa, and then formally separate that horizontal advection into its mean and anomaly components, thereby providing objective assessment to compare with the conclusions of Hu et al. (2019). The focus is on the low-level warming. However, it is recognized that in such semi-arid climate settings as the Sahel, the boundary layer undergoes a very marked diurnal cycle, and can rise to near 600 hPa at the peak of afternoon heating (e.g., Garcia-Carreras et al., 2015). Therefore, in the detailed ESL analysis, focused interest extends up to these levels.

Section 2 describes the data used, methods applied, and the selection of the case study, establishing its large-scale and local presence with observations from satellite images and ESL station observations. Section 3 starts by giving a large-scale perspective following W21 (drawing on ERA5). The section then transitions to the use of YOPP data (here, day-mean fields of standard variables), delivering insights

into the lower and upper boundary layer over northeastern Africa that assist interpretation of the dynamics temperature tendencies presented in subsequent sections. Section 4 presents a continent-scale perspective on the contribution of key tendency processes during the case study in the lower boundary layer. Section 5 provides a detailed assessment of the warming that occurs over the ESL, including the vertical profile of the tendency terms, and relating findings below 650 hPa to the diurnal cycle of the boundary layer. The functioning of near-surface and surface conditions is also considered for evidence of possible land-surface feedback. Section 6 highlights aspects that may bring nuance to this particular case study, including the role of different anomaly advection terms, potentially influenced by the approach of a cold front from the north, and conditions to the south of ESL, including storms that develop on Day 3; therefore, Section 6 introduces some secondary departures from the general evolution of the case study. Section 7 summarises conclusions.

## 2 | DATA, METHODS AND CASE STUDY SELECTION

### 2.1 | YOPP data

The YOPP dataset (Bauer et al., 2020; Jung et al., 2025) of the European Centre for Medium-Range Weather Forecasts (ECMWF) contains forecasts from the operational ECMWF integrated forecast system (IFS) model, initialized at 0 UTC each day in the period July 2017–October 2020, and available with temperature tendency attributed to physical processes at 3 hourly intervals for the first 48 h of the forecast ( $t + 0$  to  $t + 48$ ). The data are therefore well-suited for the purpose of this paper, to understand the development of low-level temperature anomalies over northern Africa.

The 3-hourly data for temperature tendency and other selected variables have been downloaded on the same grid used in T18 and W21 ( $0.75^\circ \times 0.75^\circ$ ). The model contains 91 levels, and for the longitudes of ESL, data are accessed for all levels 91–71 (the lowest level to about 650 hPa) and then every third level to 47 (about 180 hPa). For large-scale analysis at continental scale, a smaller set of key model levels were selected. Most results presented use the model level data. The exact pressure level that each model level corresponds to varies slightly according to surface pressure, and this has been accounted for in all calculations (following Bauer et al., 2020). Additionally, pressure-level (served for a few interpolated levels only), surface and special case variables were accessed as needed, the latter including boundary-layer height (BLH, meters). We have used the hypsometric relation

(see Supporting Equations S1) to translate this to its corresponding pressure height coordinate (hPa) to locate the BLH on plots using pressure as height variable.

The target case study is in February 2018, but data were downloaded for all YOPP Februaries, i.e., 2018, 2019 and 2020 (85 days). Drawing on these days to form an 85-day climatology was valuable to get a better perspective of the anomalous conditions in February 2018 (see also Section 2.3, Figure S1). Where results are presented in anomaly format, the following procedure is applied to each grid-box: the anomaly of variable  $\varphi$  at forecast hour  $t + h$  in forecast run initialized at 0 UTC on day  $d$  is calculated:

$$\varphi'(d)_{t+h} = \varphi(d)_{t+h} - \overline{\varphi}_{t+h}, \quad (1)$$

where  $\overline{\varphi}_{t+h}$  is the time-mean value of variable  $\varphi$  at forecast hour  $t + h$  ( $h = 0$  for initial conditions), with the time-mean calculated over all 85 forecasts. This leaves a small annual cycle component running through February, but this does not substantially impact results because the day-to-day anomalies focused upon are much larger. If the variable  $\varphi$  is a temperature tendency, then Equation 1 is applied with the additional referencing of  $t + h_1$  and  $t + h_2$ , where tendency is calculated from forecast hour  $h_1$  to hour  $h_2$ .

In considering the temperature tendency data, it is helpful to have in mind the Eulerian form of the thermodynamic temperature tendency equation, which can be written (Carlson, 1994):

$$\frac{\partial T}{\partial t} = \underbrace{-V \cdot \nabla_p T}_{\text{Term 1}} + \underbrace{\omega \left( \frac{R_d T}{c_p p} - \frac{\partial T}{\partial p} \right)}_{\text{Term 2}} + \underbrace{\frac{\dot{Q}_{nd}}{c_p}}_{\text{Term 3}} \quad (2)$$

where  $\frac{\partial T}{\partial t}$  is the local temperature tendency (K/s),  $-V \cdot \nabla_p T$  is the horizontal advection of temperature ( $T$ ) by vector wind ( $V$ ) on a constant pressure surface,  $\omega$  is the vertical motion (Pa/s),  $p$  is pressure,  $R_d$  and  $c_p$  are constants (gas constant for dry air and specific heat at constant pressure) and  $\dot{Q}_{nd}$  is total diabatic heating rate. The summation of Term 1 and Term 2 may be considered the tendency attributed to dynamics as served in the YOPP data (Dyna), while Term 3 encompasses the other five contributions served as temperature tendencies, namely Radiation (Radi), Turbulent Diffusion (Turb), Convection (Conv), Cloud Scheme (Clou), and parameterized sub-grid orography effects (Bauer et al., 2020; Jung et al., 2025). The tendency attributed to each of the six contributions is accumulated through the model forecast integration. Thus, the tendency over ( $h_1 = 0$ ,  $h_2 = 3$ ) for Dyna is the local change in temperature (K) attributed to dynamics from  $t + 0$  (initialization) to  $t + 3$ .

While the motivation for YOPP was polar prediction, Bauer et al. (2020) note that, since the ECMWF data are

from the global IFS, they may be studied in any region of the world. One caveat is that the model was subject to regular operational enhancement once each year during YOPP (covering model cycles 43r3, 45r1, 46r1). These system changes could potentially impact the February 2018–2020 mean values, in turn impacting the calculated YOPP anomalies (Equation 1); therefore results have been checked using the YOPP February 2018 base period and using ERA5 reanalysis. The anomalies that we emphasize stand out clearly regardless of these dataset and base period changes.

## 2.2 | ERA5 reanalysis data and trough index calculation

Use is made of ERA5 to identify the case study, and also to support interpretation of the YOPP data. Daily mean fields of ERA5 (Hersbach et al., 2020, 2023) were downloaded at  $0.75^\circ \times 0.75^\circ$  resolution over 1982–2020 (W21). ERA5 uses the same version of IFS throughout (based on 41r2), to increase homogeneity over time. Daily anomalies (using 1982–2016 base period) were calculated for each grid location, using a 31-day running mean climatology (W21). To identify strong trough days at a target longitude, a trough parameter (TP) index was calculated with averages over  $35\text{--}45^\circ \text{N}$ :

$$\text{TP} = \left( \frac{Z_1 + Z_3}{2} \right) - Z_2 \quad (3)$$

where  $Z_2$  is the average geopotential height anomaly at 200 hPa ( $Z_{200}$ ) for a  $10^\circ$  longitude zone centred on the target trough longitude, and  $Z_1$  and  $Z_3$  are average  $Z_{200}$  anomalies for the  $12.5^\circ$  zones to the west ( $Z_1$ ) and east ( $Z_3$ ) of  $Z_2$ . Large values of TP indicate the presence of a strong trough; explicitly, it measures the zonal gradient into the target trough longitude (Knippertz, 2004) and may also be considered a finite difference measure of the curvature associated with the trough. Values of TP targeting Iberia (IB) ( $Z_2$  centred at  $2.5^\circ \text{W}$ ) and Central Mediterranean (CM) ( $Z_2$  centred at  $12.5^\circ \text{E}$ ) are used (Figure 1a).

## 2.3 | Case study selection and its presence in non-ERA5 products

Although W21 found that IB and CM troughs (Figure 1a) could independently excite warming over northeastern Africa, the largest warming signal occurred with a sequence of strong IB trough, followed by strong CM trough about 2–3 days later. This heralded warming that spread southeastward to deliver particularly strong and persistent low-level warming in ESL. In W21, the 850-hPa temperature ( $T_{850}$ ) index for the ESL domain (Figure 1a)

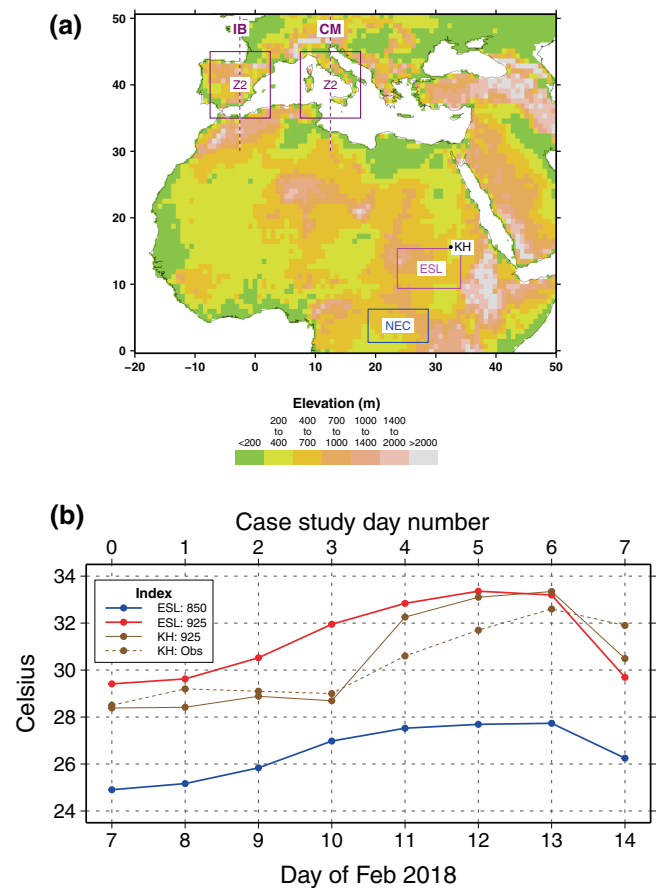


**FIGURE 1** (a) Some key locations used in the study, along with topographic elevation for reference (as constructed in W23). Target central longitude (vertical dash lines) for Iberia (IB) and Central Mediterranean (CM) upper-level trough index calculation, showing the central zone 2 ( $Z_2$ ) box (Equation 3). Domain for the eastern Sahel (ESL) temperature indices (termed N45 in W21), and location of Khartoum (KH) weather station. For reference, the domain of northeastern Congo (NEC) is also shown. Local time over ESL longitudes is approximately UTC + 2 hours. (b) Daily mean temperature evolution over ESL and Khartoum during the case study event. For ESL domain, ERA5 850-hPa temperature (blue), ERA5 925-hPa temperature (red). For Khartoum, station observations (brown dash line) and an ERA5 925-hPa approximation for Khartoum, taken to be the average of the 4 closest grid-boxes  $15.00\text{--}15.75^\circ \text{N}$ ,  $32.25\text{--}33.00^\circ \text{E}$  (brown solid line). Upper x-axis denotes the case study day number that is used in the text and other figures. [Colour figure can be viewed at [wileyonlinelibrary.com](https://onlinelibrary.wiley.com/doi/10.1002/qj.70058)]

showed strongest temperature signal at these low latitudes and also showed maximum (positive) correlation with enhanced convective activity to the south over northeastern Congo (NEC, Figure 1a). Therefore, the case study was identified based on the sequence of IB and CM troughs and ESL  $T_{850}$  tendency.

The day of the strong IB trough defines day 0. An identification procedure sought days in December–March when IB trough strength was in the top 10 percentile of



days, followed by strong (10 percentile) CM at Day 2 or Day 3, and with strong (10 percentile) ESL T850 tendency measured as the mean anomaly for Days 4–6 (relative to mean anomaly conditions in the 3 days prior to Day 0). In the period of YOPP data, Day 0 of 7 February 2018 is the only day to satisfy these criteria (IB trough Day 0,  $p = 0.06$ ; CM trough Day 3,  $p = 0.05$ ; ESL T850 tendency,  $p = 0.07$ ; where  $p$  is the percentile in the daily anomaly values over December–March 1982–2020).

For context, over 1982–2020, a total of 23 winter events are identified when applying the above strong  $p < 0.1$  criteria. The ESL T850 anomaly reached in the February 2018 event ( $+6.5^{\circ}\text{C}$ ) is the highest of those 23 events. Taking the strongest 20% of CM troughs (following the methodology in W21 and W23), the peak anomaly of  $+6.5^{\circ}\text{C}$  ranks 18 out of the 946 strong trough events. The composites of these events were extensively tested and shown to be highly statistically significant (W21, W23). Therefore, this case study can be considered a strong example from composites

that have previously been shown to be highly statistically significant.

Given the above case selection is based on ERA5 data alone, it was considered useful to seek independent validation of the presence of the major event, both its large-scale northern Africa expression and the local ESL temperature expression (including longer-term context). For the local expression, no long weather records that extend into recent years could be located within the ESL domain, but Khartoum (KH) is very close to the northeast corner of ESL (see Figure 1a), and almost complete daily surface temperature observations, served through WMO Global Surface Summary of the Day (NOAA, 1999), are available to analyse for 2011–2020. Encouragingly, both these KH data and ERA5 ESL indices agree that February 2018 is the warmest February in the decade (2011–2020) and their year-to-year variations match very closely (Figure S1).

For the case study days, evolution of the ESL low-level temperature in ERA5 data shows a steady warming

**FIGURE 2** 10 February 2018 (Day 3) at 16 UTC, as seen in large-scale satellite imagery. (a) MSG-SEVIRI (Spinning Enhanced Visible and InfraRed Imager), showing clouds (brown/orange), dust (pink/purple) and differences in surface emissivity retrieved in the absence of dust or clouds (light blue/blue). No substantial dust is interpreted in this field, and particularly relevant to the case study, none ahead of the trailing front into northeastern Africa. (b) Same as (a) but for the enhanced Meteosat IR/Visible image with color enhanced 10.8 micron brightness temperature. On the images, the thin white lines mark country boundaries, and the red and orange boxes indicate location of eastern Sahel (ESL) and northeastern Congo (NEC) domains respectively. [Colour figure can be viewed at [wileyonlinelibrary.com](https://onlinelibrary.wiley.com)]

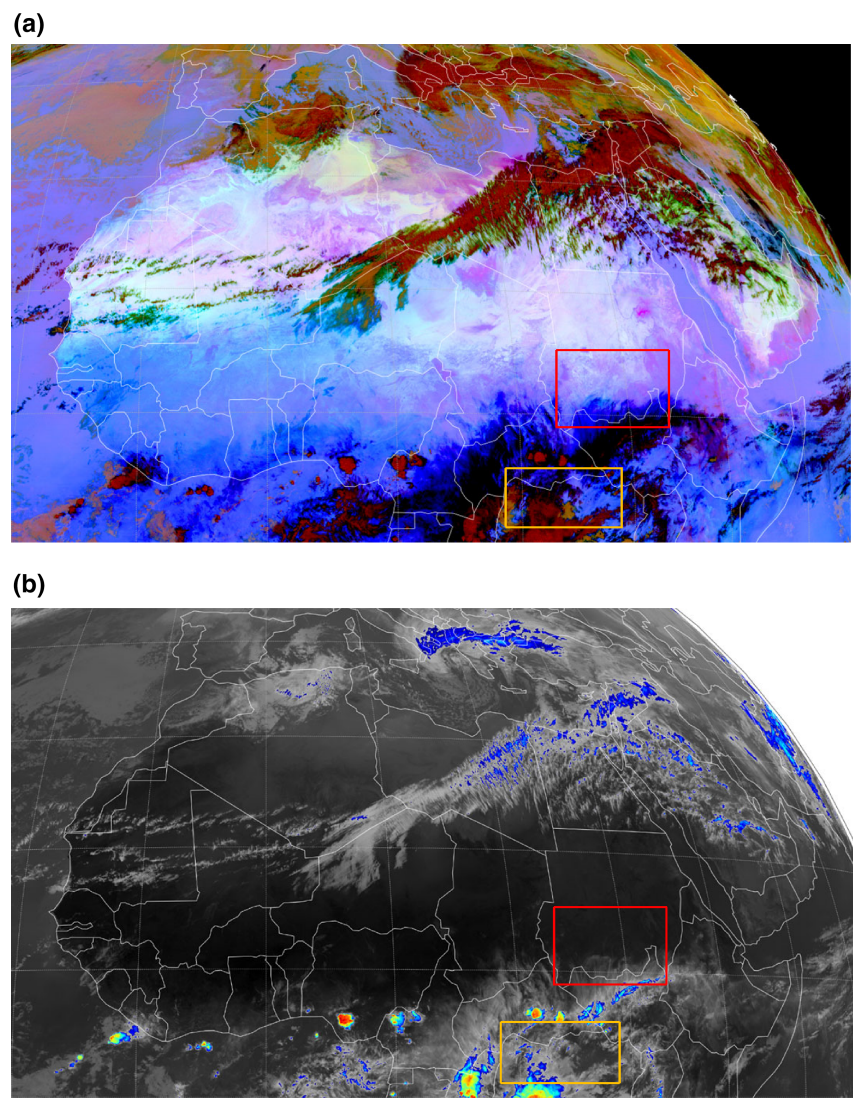


(Figure 1b), especially from Day 2 to Day 5, with the very warm conditions continuing (though not growing further) into Day 6, after which temperatures fall. This general daily evolution is also seen in the KH observations (Figure 1b); the KH index does peak slightly later (Day 6), but this is reproduced in an ERA5 925-hPa index for a smaller domain centred on KH (Figure 1b). Overall, the agreement with KH observations (Figures 1b, S1) builds confidence in the ERA5 ESL low-level temperature indices.

A large-scale perspective over northern Africa and Europe is achieved using products from Meteosat Second Generation (MSG) Spinning Enhanced Visible and Infrared Imager (SEVIRI) (see Laing et al., 2017). The products inspected were: (i) the MSG-dust product, which is an RGB (Red, Green, Blue) composite from the Infrared (IR) channels IR8.7, IR10.8 and IR12.0; the product detects many phenomena, but is specifically designed to detect dust and has been applied over the Mediterranean/North Africa (Flaounas et al., 2022); (ii) the widely-used IR color-enhanced single band 10.8 micron brightness temperature, revealing clouds and convection. Both products reveal many of the synoptic features discussed during the case study, including equatorial convection and large-scale cloud patterns over northern Africa (illustrated for Day 3 in Figure 2). The images validate the presence of a major continental-scale event, and are further referred to in subsequent sections.

### 3 | LARGE-SCALE SYNOPTIC SETTING

#### 3.1 | Northern Africa and Mediterranean continent-scale features

##### 3.1.1 | Build-up through Day 2

The days prior to Day 0 also experienced strong IB trough conditions (TP >100, percentile  $p < 0.07$ , continuously back to Day -3, still strongly positive through Day -7). Thus, the case study represents the end of a sequence that resembles the composite based on NEC highest rainfall days (W21), in which several precursor days display IB trough conditions, during which a pattern is gradually established of anomalous cool conditions in northwestern Africa and warm conditions in northeastern Africa. This pattern is therefore already in place on Day 0 of the case study (Figure 3a), with signature confined mostly to the north of 20° N.

A major Mediterranean cyclone developed in this setting (Varga, 2020, and see Figure S2a, DWD Surface Analysis). It tracked along the forward edge of the IB

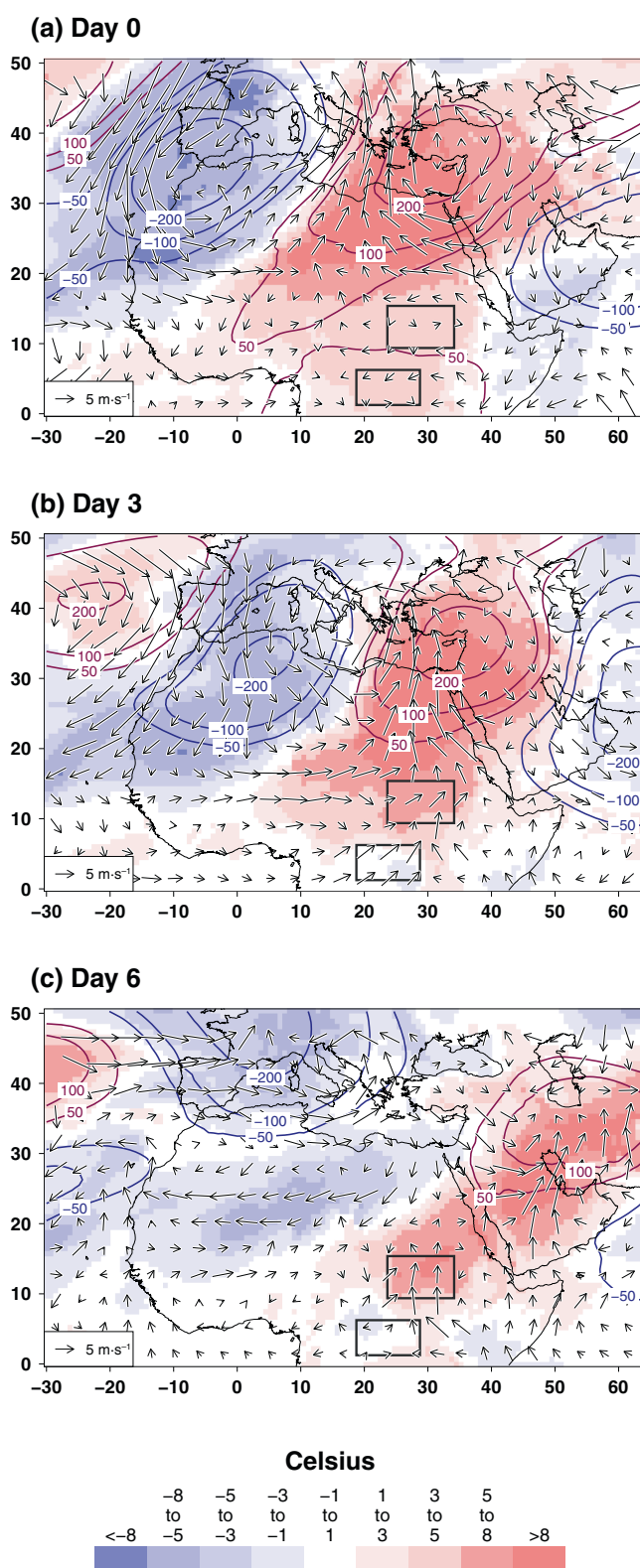


**FIGURE 3** Large-scale setting for the case study event, based on ERA5 data. (a) Anomalies for Day 0 (7 February 2018) for 850-hPa temperature (shading), 200-hPa geopotential height (contours, m) and vector wind at 850 hPa. (b) Same as (a) but for Day 3 (10 February 2018). (c) Same as (a) but for Day 6 (13 February 2018). [Colour figure can be viewed at [wileyonlinelibrary.com](https://onlinelibrary.wiley.com/terms-and-conditions)]



trough, but with the large-scale trough situation remaining almost stationary through Day 2 (IB TP still 83.2,  $p < 0.10$ ).

### 3.1.2 | Days 3–6

As the upper-level trough finally propagates eastward, reaching CM longitudes by Day 3, so another Mediterranean cyclone is spawned, which this time takes a more eastward track. The cyclonic low-level circulation is centred near 18° E on Day 3 (Figure 3b). We have confirmed that ERA5 and YOPP match closely in their treatment of this and the earlier Mediterranean cyclone (Figure S2e–h). On Day 3, the DWD Surface Analysis (Figure S2b) places a trailing cold front into North Africa, engaging and now transitioning southeastward, the large-scale west–east cold–warm contrast over northern Africa that had been set up during the persistent IB trough of the previous days.

There is a trailing high-level cloud band across northeastern Africa (Figure 2) that also reflects a persistent strong mid-level moisture plume (see Figure S3a–f) associated with the earlier persistent IB trough (consistent with Knippertz & Fink, 2008). The cloud band subsequently tracks the progression of the cold front (not shown). However, for this particular event, the mid-level ridge over Arabia is strongly persistent, and does not allow the moisture plume to penetrate south and east during Days 3–5 (see Figure S3a–c). It is not until the Arabia ridge fully decays around Days 8–10 that strong positive moisture anomalies become established over ESL (see Figure S3e,f).

By Day 3, the strongest positive temperature and southerly wind anomalies are over 20–35° E, now extending from ESL latitudes northward into the Mediterranean region (Figure 3b). The wind anomalies established over and to the north of ESL on Day 3, continue through Days 4–5 over ESL (see Section 4.1), with further continued warming, making Days 3–5 most representative of the event over ESL. The trailing cold front continues to transition southeastward on these days (e.g., Figure S2c,d); the existence of the cold front is likely not needed for the overall warm event, but nonetheless, it does add nuance to the evolution (see Section 6.1).

During winter months, Tucker and Pedgley (1977, hereafter TP77) found almost all cold fronts in the Nile Valley were originally trailing from a Mediterranean cyclone with a nearby upper-level trough. However, warm dusty khamsin weather (Al-Mutairi et al., 2023; Goudie, 1983; Morales, 1980) was not prevalent in winter ahead of the front, when any dust activity was behind the front in enhanced gusty northerly winds. This makes a role for radiative impacts from dust in the warming process unlikely, and indeed, for the case study, there is no dust evident in the satellite dust product on Days 3–5

(illustrated for Day 3, Figure 2a). By Day 6 (Figure 3c) the low-level advection discontinuity (see TP77), that marks the remnants of the cold front, approaches ESL. Furthermore, near-surface temperatures over ESL cease to rise further from Day 5 (Figure 1b), confirming Days 3–5 as the key ones to understand for the warm event over ESL.

## 3.2 | Days 3–5 low-level features over northeastern Africa and climatological context

This section builds context for interpretation of the tendency process results (Sections 4–5). Also, by now using YOPP day-mean standard fields (Figure 4), it establishes the YOPP data's general consistency with the ERA5 day-mean discussion (Section 3.1). In the low-to-mid boundary layer, climatological wind over northern Africa is marked by the well-known Harmattan, winds with a northerly component, generally effecting cold advection, extending in latitude from the northern Sahara southward to near the intertropical discontinuity (ITD), and in longitude from the Atlantic to the Red Sea / Ethiopian Highlands (see Fink et al., 2017; Lavaysse et al., 2009). These winds are particularly strong with northerly component on the eastern side of the continent and especially over ESL longitudes. They operate on a strong meridional temperature gradient to effect cold advection (the low-level wind and temperature climatologies are at Figure 4a,b). This mean cold advection becomes interrupted from northern Egypt to the southern border of ESL during the case study Days 3–5 (Figure 4d,e, fields that are consistent with ERA5, Figure 3b). Therefore, modified temperature advection is a prime candidate to account for the temperature tendencies at these levels.

This situation dramatically contrasts with conditions at 700 hPa (Figure 4c,f). Climatological wind is weak at ESL latitudes, with prevailing westerlies extending northward to the Mediterranean, and with near-zero meridional component. Therefore, there is no climatological cold meridional temperature advection to be perturbed at this 700-hPa level. Moreover, wind anomalies associated with the upper-level trough are also very weak at ESL latitudes (Figure 4f).

## 4 | THE DAY-MEAN LOW-LEVEL TEMPERATURE TENDENCY FIELDS OVER NORTHERN AFRICA

This section summarizes the temperature tendency fields in the low-to-mid boundary layer. After experimentation, model level 83 (about 890 hPa over ESL) is used to give

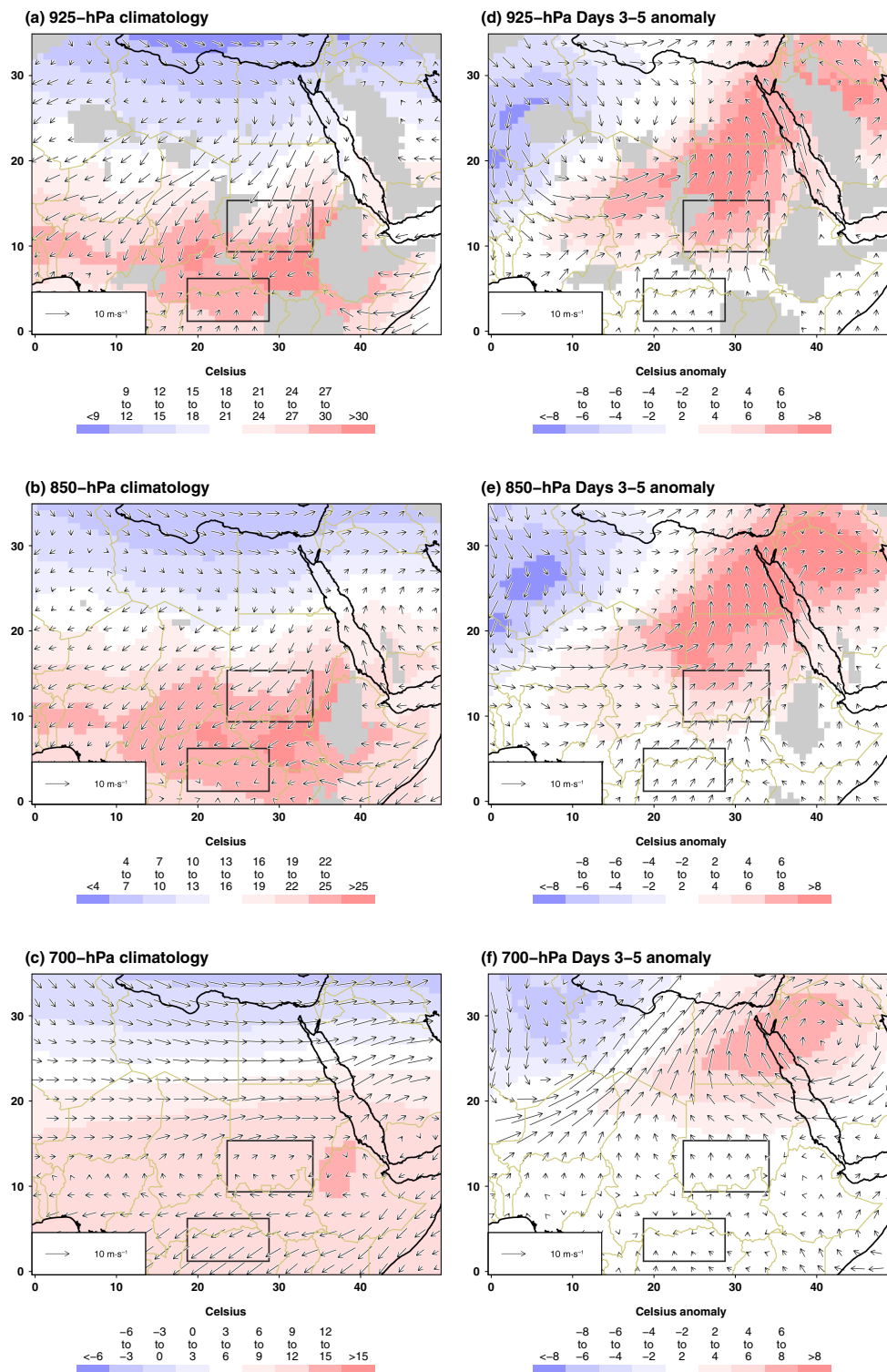


**FIGURE 4** (a) 925-hPa vector wind and temperature averaged over the 85 February days available in the ECMWF YOPP 24-hour forecast archive (i.e., averaged over February 2018, 2019 and 2020). The southern gray box marks the NEC domain, while the gray box to its northeast marks the ESL domain (see Figure 1a). (b) Same as (a) but for 850 hPa. (c) Same as (a) but for 700 hPa. (d) Same as (a) but now the mean anomaly (relative to the 85-day climatology) for Days 3–5 of the case study (i.e., 10–12 February). (e) Same as (d) but for 850 hPa. (f) Same as (d) but for 700 hPa. For visual clarity, wind vectors are averaged into  $2.25^\circ \times 2.25^\circ$  boxes (i.e., averaging the 9 constituent  $0.75^\circ \times 0.75^\circ$  boxes). Shaded fields are masked gray whenever a grid-box is estimated to be below the surface based on the YOPP day-mean surface pressure values. Similarly, wind vectors are removed from the plot if >50% of the vector's constituent boxes were estimated to be below the surface. Light brown lines indicate country boundaries. [Colour figure can be viewed at [wileyonlinelibrary.com](https://onlinelibrary.wiley.com/doi/10.1002/qj.70058)] [wileyonlinelibrary.com](https://onlinelibrary.wiley.com/doi/10.1002/qj.70058)]

a representative indication for much of northern Africa (Section 5 details ESL at all levels). Also, discussion is confined to the terms that determine the bulk of the tendency during the case study (Dyna, Turb and, to a lesser extent, Radi).

#### 4.1 | Dynamics tendency (Dyna)

The large-scale evolution of low-level anomalous Dyna during the case study (Figure 5) reveals a northern Africa continental-scale sequence. For Day 0 (Figure 5a),



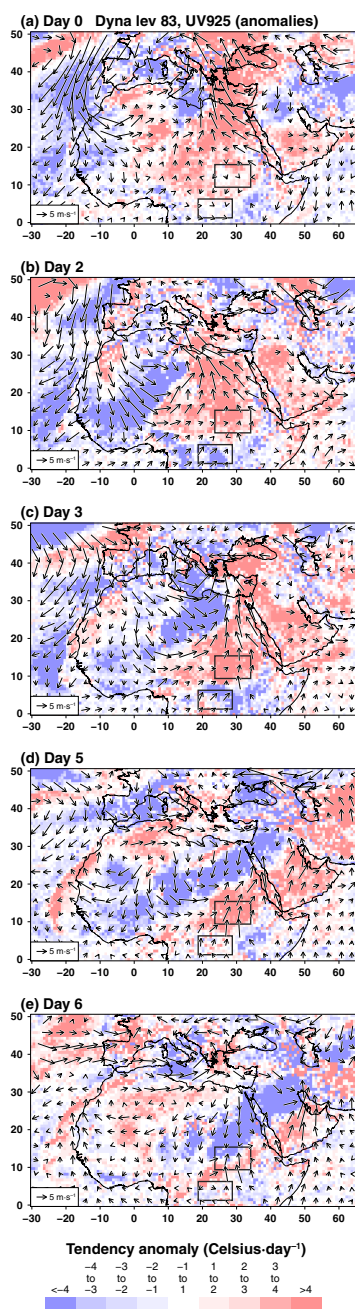


**FIGURE 5** (a) The 24-hour temperature tendency anomaly at model level 83 attributed to dynamics (shading) for the forecast initialized at 0 UTC on 7 February 2018, i.e., Day 0 in the case study sequence. Level 83 represents about 890 hPa over ESL. Also shown is the 7 February 2018 day-mean low-level vector wind anomaly (925 hPa) as served in the YOPP data pressure level archive of the forecasts. Anomalies are relative to the 85-day climatology formed from model forecasts on each February day, 2018–2020. The southern gray box marks the NEC domain, while the gray box to its northeast marks the ESL domain. (b) Same as (a) but for 9 February 2018 (Day 2). (c) Same as (a) but for 10 February 2018 (Day 3). (d) Same as (a) but for 12 February 2018 (Day 5). (e) Same as (a) but for 13 February 2018 (Day 6). Wind vectors processed as in Figure 4, except now at  $3.75^\circ \times 3.75^\circ$  resolution. [Colour figure can be viewed at [wileyonlinelibrary.com](http://wileyonlinelibrary.com)]

when the near-stationary IB trough prevails, anomalous warming tendency is found over northeastern Africa, weaker but nonetheless present down to ESL latitudes. It is noticeable that low-level horizontal wind anomalies are near zero at ESL latitudes, suggesting a role for vertical motion in the slow Dyna warming (see Section 5.5).

Over northwestern Africa during Day 0, anomalous Dyna cooling generally prevails (Figure 5a), but with some detail, likely reflecting the Mediterranean cyclone ahead of the IB trough (see Section 3.1). By Day 2 (Figure 5b) the dynamics are becoming more organized at the large scale, with a strong boundary between anomalous Dyna cooling and Dyna warming extending from close to the Mediterranean coast in northern Libya, southwestward to the equatorial latitudes of northern Ghana. To the west of that Dyna cooling/warming boundary, strong northwesterly low-level wind anomalies are consistent with enhanced cold advection. In contrast, anomalous Dyna warming and anomalous southerly wind extends over much of northeastern Africa, now with moderate warming extending southward to ESL.

It is on Day 3 (Figure 5c) that anomalous Dyna warming over ESL becomes established at its strongest levels, with southerly wind anomalies now extending to ESL latitudes. This situation continues through Day 5 (Figure 5d). Averaged over Days 3–5, the anomalous Dyna warming tendency (Figure 6d) clearly represents a strong reduction of the climatological Dyna cooling over this region (see Dyna climatology, Figure 6a). Inspection of Figure 4 suggests the anomalous Dyna warming tendency (Figure 6d) represents anomalous meridional advection. However, consistent with Figure 4, these tendency features are focused in the lowest levels, and by 700 hPa (Figure S4d) they are absent.

The anomalous low-level Dyna cooling to the north (Figure 6d) occurs close to the frontal boundary; inspection of the northerly wind anomalies suggests horizontal advection (Equation 2, Term 1) may not be sufficient to explain all the anomalous Dyna cooling, pointing to a possible role for vertical motion (Equation 2, Term 2) in this anomalous cooling tendency (as speculated by TP77 for Nile cold fronts). This interpretation is reinforced by the continued existence of Dyna cooling in the vicinity of the front above 850 hPa (Figure S4d), where it forms the main Dyna tendency feature at that level in the region.

During Days 3–5 at low levels (Figure 5c,d), the boundary of anomalous Dyna cooling and warming advances consistent with the earlier synoptic discussion (Section 3), and strongly extends to the Arabian Peninsula. The boundary enters ESL at the lowest levels on Day 6 (Figure 5e), which is marked by much stronger low-level ascent over ESL than any other case study day (Figure S8).



## 4.2 | Turbulence tendency (Turb)

Considering similar continent-wide anomaly maps for Turb (Figure S5a–e) reveals a general first order damping of the low-level Dyna anomalies by the Turb anomalies. Climatologically, Turb is warming the lower boundary layer over the Sahel and Sahara (Figure 6b). During the warm event, Turb is less effective, and this leads to a damping of the warm anomaly (Figure 6e). In opposite sense, where enhanced cold advection anomalies appear to be operating behind the cold front (Figure 6d, near 15–20° N, 0–10° E) so the climatological warming tendency of Turb is enhanced to deliver positive anomalies (Figure 6e). Over northern Egypt across Days 3–5, there are no Turb anomalies of substance damping the Dyna cooling anomaly (Figure 6d,e), again suggestive of a different mechanism arrangement close to the front (hypothesized to involve vertical motion).

## 4.3 | Radiation tendency (Radi)

Ahead of the front, in the warm dry air, Radi generally operates (Figure S6a–e) to provide a further damping to the anomalous Dyna warming (Figure 5). The magnitudes are about 3 times smaller than Turb (Figure S5), but the signal is clear over Days 3–5 (Figure 6f), corresponding to an increase in the climatological cooling role for Radi at this level (Figure 6c). The way the patterns track the broad-scale moisture (Figure S3) is indicative of a role for water vapour anomalies perturbing night-time cooling (detailed for ESL in Section 5.3). Figure S4a–f (near 700 hPa) provides a summary of the contrasts with the lower boundary-layer Dyna, Turb and Radi features (Figure 6a–f); the vertical profile contrasts are discussed in detail for ESL in the next section.

# 5 | TENDENCY MECHANISMS OVER ESL: VARIATIONS WITH HEIGHT

## 5.1 | Days 3–5: Dynamics (Dyna) and turbulence (Turb)

The ESL anomaly vertical profile of each tendency term (Figure 7) confirms that for levels up to about 850 hPa, the primary impression from Figure 6d,e prevails, with anomalous Dyna warming, and partial damping from Turb.

Higher up, between 825 and 650 hPa, the Dyna anomaly reverses sign (returned to in Section 5.2), while Turb now contributes anomalous warming that is large

enough to deliver an overall continued net warming to near 650 hPa (Figure 7). Typically, the BLH reaches about 750 hPa in the afternoon (Figure 8a), however, during the anomalously warm Days 3–5, the BLH reaches near 650 hPa (Figure 8a), which is the level on Figure 7 that the anomalous Turb warming reaches.

Therefore, it is proposed that the anomalous Turb warming is attributed to mixing (feeding on the low-level warm anomalies) during the afternoon BLH extension into the 825–650 hPa zone. To support this interpretation, the afternoon 3-hour tendency profile (Figure 9a) shows very clearly the anomalous Turb warming 825–650 hPa, and this is absent or trivial at other times of the day (e.g., Figure 9b–d).

Above 650 hPa, tendency anomalies are relatively small (Figure 7) and not considered indicative of primary processes that contribute to the low-level warming on these days. However, there may be repeating signatures occurring during the warm event, to be checked in future studies, such as the anomalous cooling tendency near 600 hPa, contributed to by Dyna, Clou, and Radi, and partly damped by Conv (Figure 7).

## 5.2 | Days 3–5: Dynamics (Dyna) due to horizontal and vertical motion

To better understand Dyna, it is helpful to separate it into tendency attributable to horizontal advection (Equation 2, Term 1, hereafter Dyna(hori)) and vertical motion (Equation 2, Term 2, hereafter Dyna(vert)); the sum of these two terms is the served YOPP Dyna. Dyna(vert) has been estimated (Equation 2) using finite difference approximations across the vertical model levels (see Supporting Equations S2). Horizontal winds on constant pressure surface are not available for the model levels, but Dyna(hori) can be estimated as the difference between Dyna(vert) and the YOPP Dyna. To provide a further estimate of Dyna(hori) at 850 hPa, a horizontal advection analysis has been undertaken using 850-hPa ERA5 data (see Supporting Equations S3 and Figure S7a–f).

The ESL climatology (Figure 10a) shows that Dyna and Dyna(vert) are very similar through the bulk of the free troposphere (200–800 hPa) suggesting the Dyna(vert) warming tendency makes the main contribution to the winter climatology of Dyna at these levels. Below 850 hPa (Figure 10a), Dyna is very large and negative, while Dyna(vert) is small (consistent with a well-mixed boundary layer), implying Dyna(hori) contributes the vast majority of the negative Dyna climatological tendency in these low levels.

Over Days 3–5 in the case study (Figure 10b), the climatological low-level Dyna cooling is dramatically reduced,

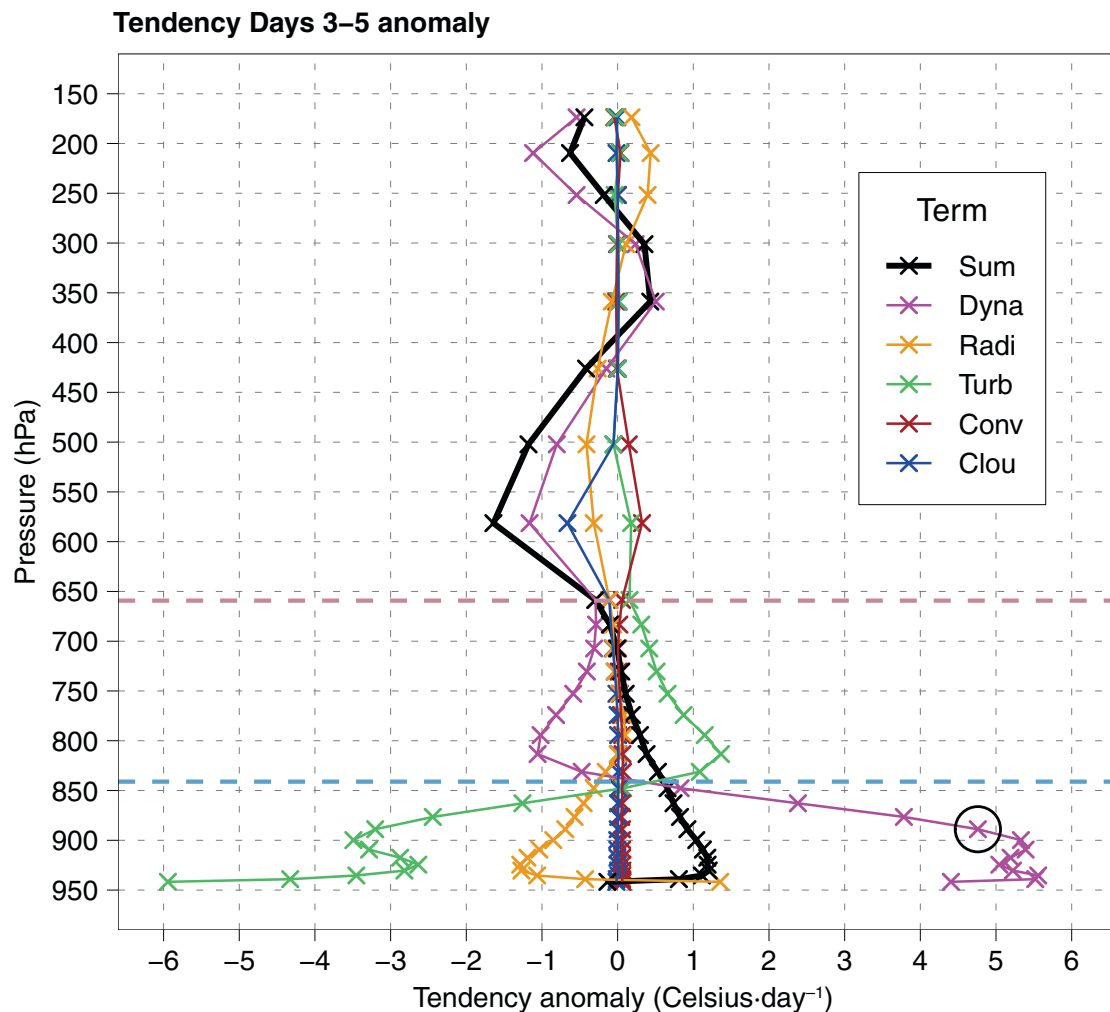


**FIGURE 7** Area-average over ESL for the 24-hour temperature tendency anomaly attributed to each tendency term. The 24-hour tendency anomaly is averaged for forecasts initialized at 0 UTC on 10 February, 11 February and 12 February 2018. This gives the mean signature during the strongest days of low-level warming during the case study (Days 3–5). Anomalies are relative to the 85-day climatology formed from model forecasts on each February day, 2018–2020. The terms plotted are tendencies attributable to dynamics (Dyna), radiation (Radi), turbulent diffusion (Turb), convection (Conv), and the cloud scheme (Clou). Contribution from the remaining term, sub-grid orography, is trivially small here, and is dropped from the plot. The summation of all terms (Sum) gives the net 24-hour tendency anomaly predicted by the model. The circled value highlights model level 83, which is used in plots (e.g., Figure 5) to illustrate the low-level signature. For context, boundary-layer height information averaged for Days 3–5: Pink horizontal dashed line is the boundary-layer height averaged over 12 UTC and 15 UTC; light blue dashed horizontal line is the day-mean boundary-layer height. [Colour figure can be viewed at [wileyonlinelibrary.com](https://onlinelibrary.wiley.com/doi/10.1002/qj.70058)]

with very large positive tendency anomalies below 875 hPa. These anomalies are attributed to Dyna(hori); anomalies of Dyna(vert) are five times smaller than Dyna, and in fact, of mostly opposite sign, therefore acting to modestly damp the driving Dyna(hori). Higher up, by 850 hPa, Dyna and Dyna(vert) continue to have opposite sign, but have now become comparable in magnitude (Figure 10b), with Dyna(vert) about  $-1^{\circ}\text{C}/\text{day}$ , and Dyna about  $+1^{\circ}\text{C}/\text{day}$ ; this implies a Dyna(hori) of about  $+2^{\circ}\text{C}/\text{day}$  at 850 hPa. Encouragingly, this is consistent with the estimate of 850-hPa Dyna(hori) based on the ERA5 ( $+2.34^{\circ}\text{C}/\text{day}$ , brown dot on Figure 10b),

with the meridional advection component dominant ( $+3.02^{\circ}\text{C}/\text{day}$ ); indeed there is a small damping by zonal advection ( $-0.68^{\circ}\text{C}/\text{day}$ ) (see Figure S7a–f for maps of ERA5 advection estimates, including zonal and meridional separation).

Over 800–650 hPa, Dyna and Dyna(vert) are very similar (Figure 10b), ranging about  $-1.2^{\circ}\text{C}/\text{day}$  near 800 hPa to  $-0.3^{\circ}\text{C}/\text{day}$  at 650 hPa. Therefore, the presence of the negative Dyna anomalies over these levels on Figure 7 is attributable to Dyna(vert), related to anomalous ascending motion that is present from near-surface to 650 hPa (illustrated for Day 4, Figure S8).



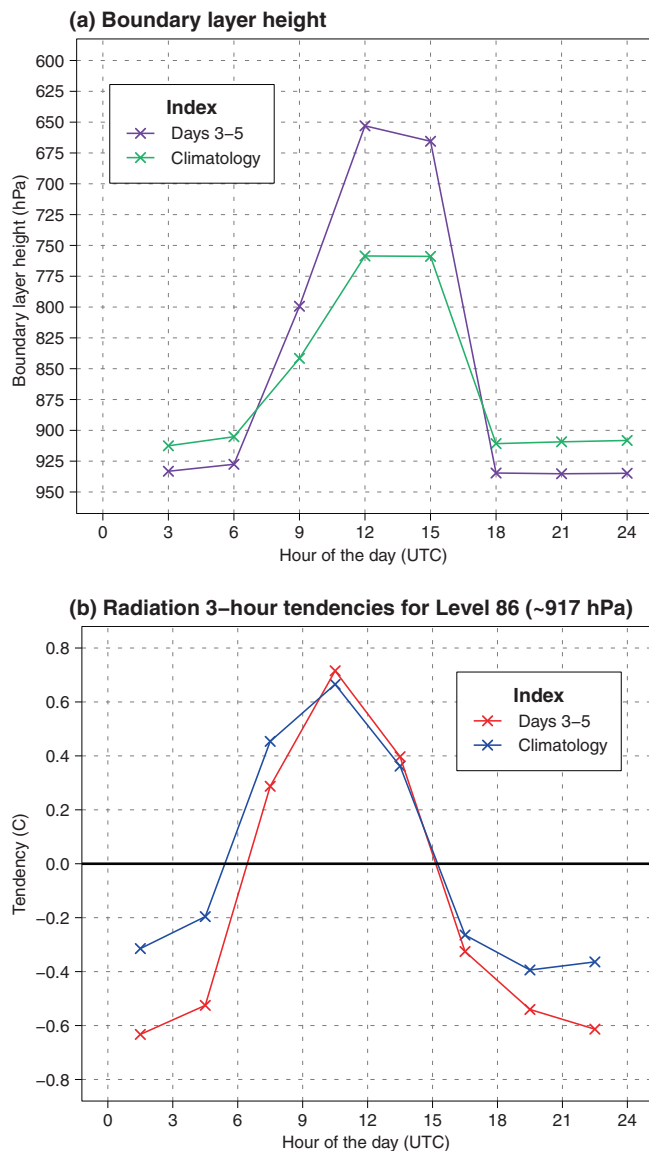


**FIGURE 8** (a) Boundary-layer height diurnal cycle averaged over ESL for the 85-day February climatology (green line) and for the mean of forecasts for 10 February, 11 February and 12 February 2018 (i.e., Days 3–5 of the case study) (purple line). (b) Same as (a) but for 3-hour temperature tendency attributable to radiation at Level 86 (representing about 917 hPa over ESL), climatology (blue line) and Days 3–5 (red line). Local time over ESL longitudes is approximately UTC + 2 hours. [Colour figure can be viewed at [wileyonlinelibrary.com](https://onlinelibrary.wiley.com)]

For the aims of this paper, the main finding is that the dominant driving of the low-level warming is horizontal advection. The reasons for the small damping by anomalous ascending motion are beyond the scope of this paper. However, an avenue for future research could assess whether during the warm event (Days 3–5), boundary-layer conditions move closer to the situation presented in detail for summer West Africa (Parker et al., 2005) and southern Africa (Attwood et al., 2024),

in the vicinity of heat lows. In such situations, during the day, dry convection maintains a warm boundary layer which has a tendency to ascend on the large scale, however the convective turbulence also suppresses convergent winds, therefore limiting the strength of this ascent (e.g., Parker et al., 2005). At night, the low-level winds are free to converge, and large-scale ascent of the residual boundary layer (Garcia-Carreras et al., 2015; Oke, 1987) may continue to occur; over time, this leads to adiabatic cooling and a weakening of the pressure gradients, with Attwood et al. (2024) showing that vertical motion may persist until around midnight. Indeed, the anomalous cooling associated with anomalous ascent over ESL over Days 3–5 at 850–650 hPa occurs most clearly in the late evening into early overnight hours (see Figure 9b,c). Specific Dyna(vert) plots (not shown) confirm the 850–650 hPa Dyna anomalies in Figure 9b,c are primarily attributable to Dyna(vert), as in the day-mean results (Figure 10b).

### 5.3 | Days 3–5: Radiation (Radi) (not near-surface)

Away from very close to the surface, up to about 825 hPa, the Radi tendency anomaly is negative (Figure 7) and therefore represents a further damping on the warm event. This damping in the large-scale maps appeared to track ahead of the cold front where the air was anomalously dry (Section 3), suggesting a reduced night-time greenhouse effect as a candidate to explain the damping.

In support of that explanation, the negative Radi anomaly is confined to over-night hours (Figure 8b). It is possible that other events with a tropical moisture plume over ESL will show Radi making a positive contribution. However, the results of this case study here (e.g., Figure 8b) confirm that a major warming following mid-latitude troughs does not require that such a moisture feedback be engaged.

### 5.4 | Days 3–5: Lowest-levels Radi, surface variables and diurnal cycle

This section considers the evolution of conditions over ESL at or very near the surface. First, we address the surprising absence of positive net tendency anomaly for the lowest model layer (about 3.5-hPa thick) over the ESL (Figure 7). This appears attributable to an aspect of initialization for these extremely warm days. This is implied because calculating tendencies using the  $t + 24$  to  $t + 48$  time-frame of the forecasts (i.e.,  $h1 = 24$  and  $h2 = 48$ , see Equation 1) and validating on Days 3–5, the net near-surface tendency problem is no longer present

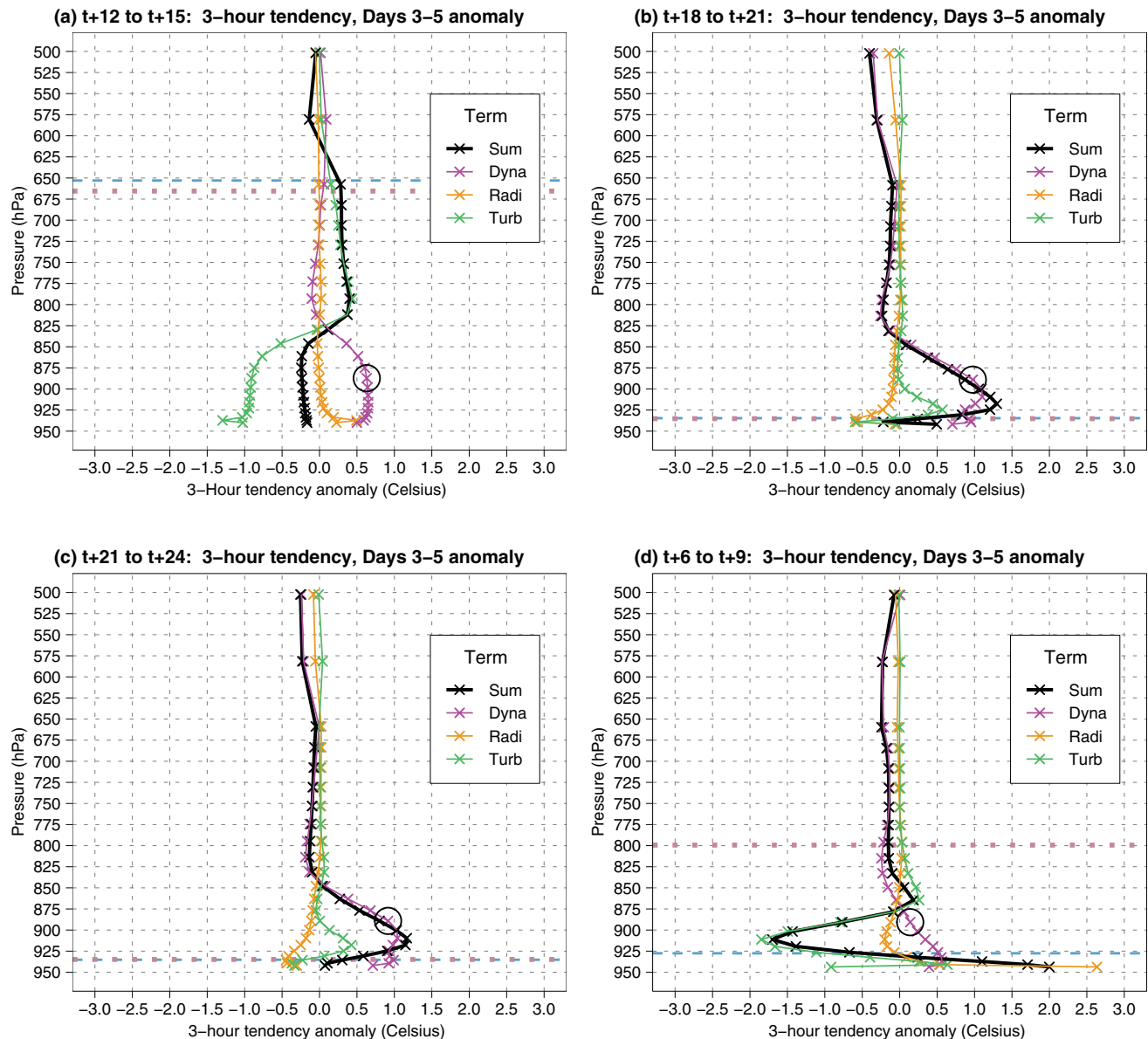


**FIGURE 9** Same as Figure 7, but for selected 3-hour tendency windows through the day (and for clarity, here not showing Clou and Conv tendencies). (a) Tendency anomaly for  $t + 12$  to  $t + 15$ , (b) Tendency anomaly for  $t + 18$  to  $t + 21$ , (c) Tendency anomaly for  $t + 21$  to  $t + 24$ , (d) Tendency anomaly for  $t + 6$  to  $t + 9$ . Local time over ESL longitudes is approximately UTC + 2 hours. For context, boundary-layer height information averaged over 10–12 February 2018 (Days 3–5): Blue dashed line is the start of the 3-hour period, and pink dotted line is the end of the 3-hour period; for example, in (a) blue dashed line (pink dotted line) is for 12 UTC (15 UTC). [Colour figure can be viewed at [wileyonlinelibrary.com](http://wileyonlinelibrary.com)]

(Figure S9c), with smooth transition of positive tendency anomalies down to the lowest model level. The tendencies near the surface and indeed through the depth of the atmosphere validate well with the “observed” tendency implied by the forecast analyses at 0 UTC (Figure S9d, see near-surface contrast for  $h1 = 0$  and  $h2 = 24$ , Figure S9a,b). Furthermore, and most relevant for this paper, the attribution of the warm event to tendency processes is almost identical regardless of whether we use the first 24 hours of the forecast ( $h1 = 0$  and  $h2 = 24$ , Figure 7) or the second

24 hours of the forecast ( $h1 = 24$  and  $h2 = 48$ , Figure S9c). This is considered a strong endorsement of the methodology being adopted, and suggests the lowest model layer issue is not critical for the overall attribution of processes. This has been found true for all results presented. For example, results for the other near-surface and surface features discussed below (Figure 11, based on the first 24 hours of the forecast) are essentially identical to results based on the second 24 hours of the forecast (Figure S10a–e).

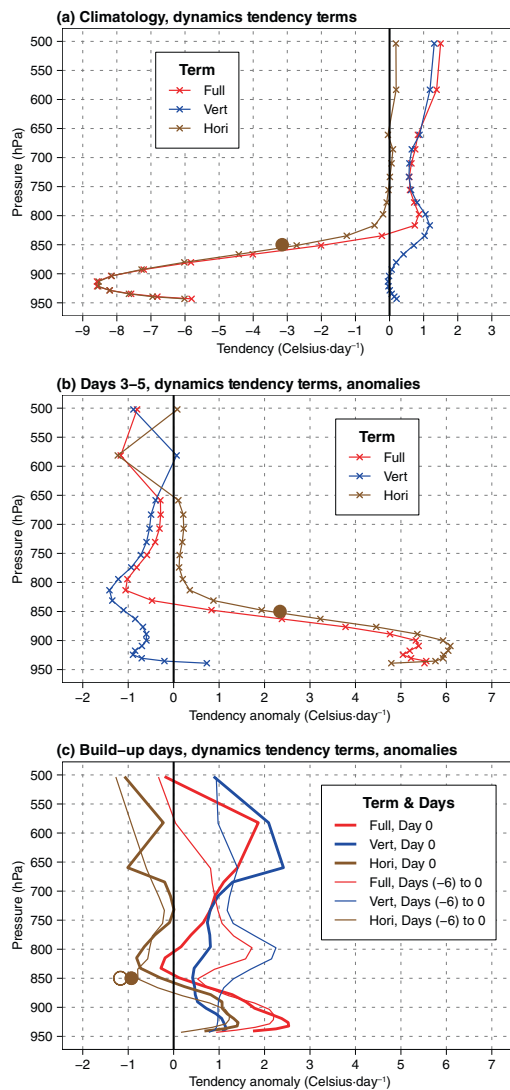


**FIGURE 10** (a) February climatology (85-days, 2018–2020), averaged over the ESL domain, for (i) the 24-hour temperature tendency attributed to dynamics as served by YOPP (red line, Full); (ii) the 24-hour temperature tendency estimated as attributable to vertical motion in the YOPP forecasts (blue line, Vert); (iii) the difference between (i) and (ii), interpreted as the 24-hour temperature tendency attributable to the horizontal temperature advection (brown line, Hori). The brown dot is the ERA5 estimate (February 2018–2020) based on 850-hPa horizontal advection analysis. (b) Same as (a) but for the mean anomaly of the 24-hour tendency values for Days 3–5 (10–12 February 2018). Hence, these values are calculated in the same way as for Figure 7, and the red line here (“Full”) is identical to the magenta line (“Dyna”) in Figure 7, except the lowest and highest model layer is omitted to match the “Vert” profile (since Vert requires vertical finite difference calculations, such that estimates of Vert are not available for the lowest and highest model layers). (c) Same as (b) but illustrating conditions in the build-up to Days 3–5, showing 7 February 2018 (Day 0, thick lines and filled brown dot) and mean of 1–7 February (thin lines and open brown dot). [Colour figure can be viewed at [wileyonlinelibrary.com](https://onlinelibrary.wiley.com/doi/10.1002/qj.70058)]

The Radi tendency anomaly in the lowest model layer is positive (Figure 7). This positive tendency anomaly occurs exclusively in the morning daylight hours (Figure 11a). These hours also mark key developments at the surface. This is the time of strongest sensible heat anomalies warming the surface (Figure 11b), with skin temperature anomalies (Figure 11c) rising rapidly from 6 to 9 UTC, consistent with the positive anomalies of implied upward thermal radiation (Figure 11d) that is a candidate to drive the positive anomaly in lowest level Radi (Figure 11a).

This chain of morning developments is preceded by the build-up of heat overnight at levels just above the night-time boundary layer, when anomalous warm advection continues, but with zero or very little Turb anomaly damping (Figure 9b,c, 925–875 hPa). After sunrise, this zone of warmth build-up experiences reset by Turb cooling (Figure 9d). While it seems likely this is related to the strong evolution of surface and near-surface features over these hours (Figure 11a–d), this will require more detailed investigation of boundary-layer processes and may require data at finer temporal resolution than 3 h to trace the causal developments. Nonetheless, the developments may be considered part of the land surface moving towards equilibrium with the prevailing anomalous warm advection, with strongest anomalous near-surface tendencies during the morning hours (following the overnight build-up of heat due to the anomalous warm advection above the nocturnal boundary layer).

Incoming solar radiation is not perturbed through the warm event (not shown) so anomalous land surface heating is not present through that mechanism. A further potential role for land-surface feedback would be associated with an anomalously dry land surface, leading to positive anomalies of latent heat (i.e., less cooling). However, in ESL at this time of year, surface moisture levels are extremely low, such that latent heat flux and latent heat flux anomalies are an order of magnitude smaller than those of sensible heat flux (compare Figure 11b,e). Therefore, we do not find at this stage evidence for a feedback role of the land surface in this type of warm event, rather, it appears as a participant in the land surface—boundary-layer atmosphere system moving towards equilibrium with the prevailing several days of anomalous low-level warm advection.

## 5.5 | Build-up through to Day 0: Dynamics tendency contrasts with Days 3–5

Section 4.1 (Figure 5a) noted modest low-level anomalous Dyna warming on Day 0 over ESL, even though the low-level wind anomalies were very different from

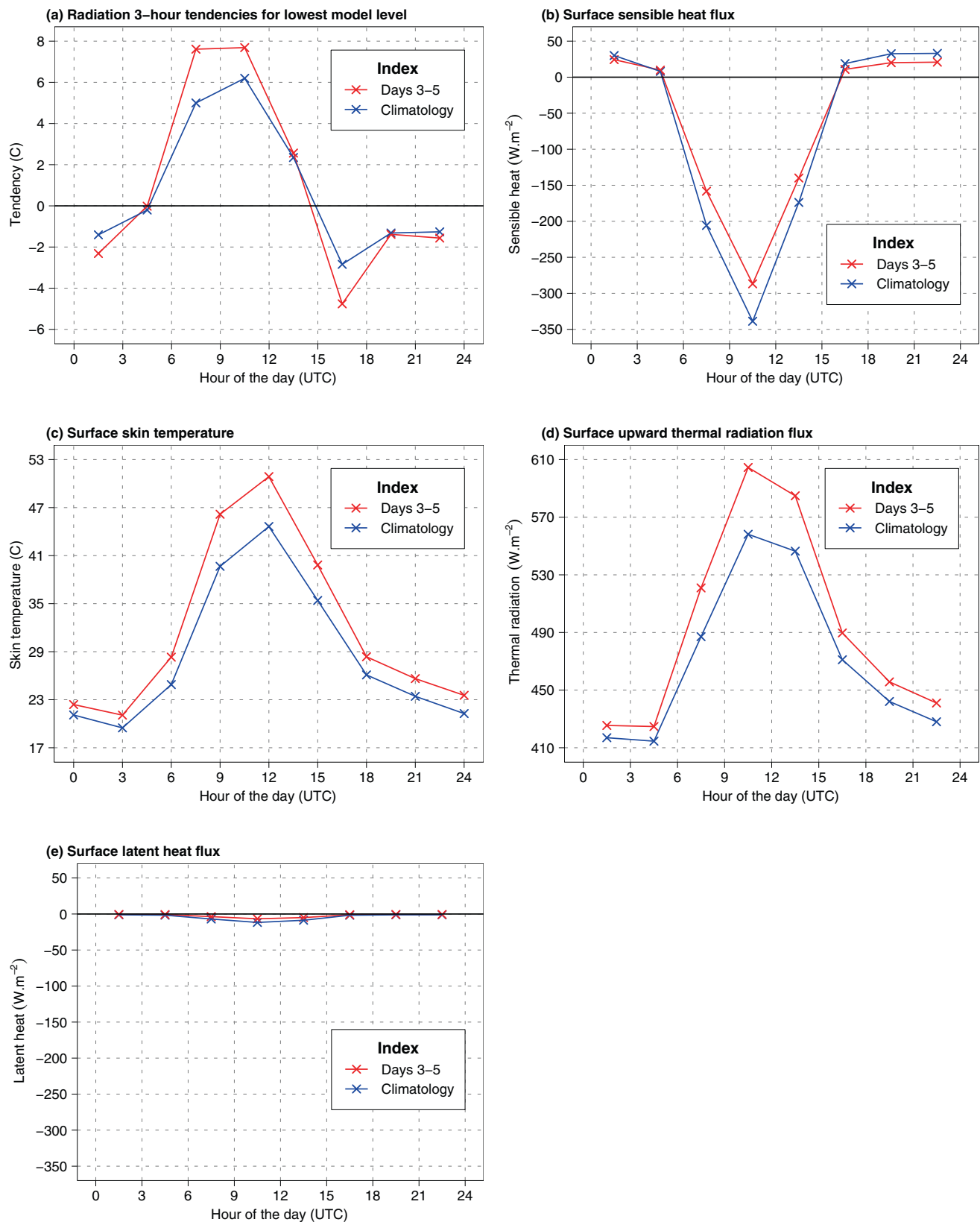


**FIGURE 11** Same as Figure 8b, but for (a) 3-hour tendency due to radiation at Level 91 (the lowest model layer), (b) Surface sensible heat flux, (c) Surface skin temperature, (d) Surface upward thermal radiation flux, (e) Surface latent heat flux. Note all values plotted are actual values, so the anomaly is the difference from the blue line, and the anomaly tendency is the rate at which the anomaly changes through the day (hence the negative anomaly tendency of skin temperature in the afternoon into early evening, essentially temperature cooling down faster than normal). Local time over ESL longitudes is approximately UTC + 2 hours. [Colour figure can be viewed at [wileyonlinelibrary.com](https://onlinelibrary.wiley.com/doi/10.1002/qj.70058)]



those on Days 3–5. Applying the Dyna separation procedure to Day 0 fields (Figure 10c, thick lines), Dyna(vert) and Dyna(hori) both contribute about  $+1^{\circ}\text{C}/\text{day}$  from near-surface levels to 875 hPa. Therefore, here Dyna(vert) contributes half of the warming, in contrast to Day 3–5, when it damps the warming.

Above 875 hPa, Dyna(hori) becomes weakly negative, a switch supported by the ERA5 Dyna(hori) estimate (Figure 10c). However, more notably above 875 hPa, Dyna(vert) continues to contribute positive tendency anomaly of typically  $+0.5$  to  $+2^{\circ}\text{C}/\text{day}$  through 500 hPa (Figure 10c) and in fact, up to 200 hPa (not shown), implying amplification of the climatological Dyna(vert) warming signature (Figure 10a). The Dyna(vert) anomalous warming signature is consistent with Day 0 anomalous descent (Figure S8). Anomalous low-level winds (Figure 5a) are near-zero over ESL, while southeasterly anomalies are established just to the north, delivering a generally divergent pattern over ESL consistent with anomalous descent, while at upper-levels, the anomalous descent driving Dyna(vert) is occurring in the presence of the downstream upper-level ridge extending southward towards ESL (Figure 3a).

The profiles for Day 0 (Figure 10c) contrast greatly with Days 3–5 (Figure 10b), revealing a very different Dyna signature on the IB trough day. Indeed, as noted in Section 3, strong IB trough conditions generally prevailed through 1–7 February, and the mean over these days (Figure 10c, thin lines) reproduces much of the 7 February (Day 0) signature, especially Dyna(vert) anomalous warming. Conditions on Days 1–2 (not shown) over ESL display transition from the profiles in Figure 10b,c.

## 6 | SOME INTRA-EVENT SPECIFICS DURING THE CASE STUDY

### 6.1 | Horizontal advection terms over ESL

Section 5 found that for the key Days 3–5, the primary contributor to the ESL warm event was anomalous low-level meridional temperature advection. This is consistent with Hu et al. (2019) where it was proposed through inspection of temperature and wind fields that the temperature advection anomaly resulted primarily through the full wind (mainly northerly) operating on the anomalous meridional temperature gradient, especially in the mature phase of the warm events they analyzed. This can be explored in more detail by breaking out the meridional advection, following standard procedure, into its climatological and anomalous components (see Supporting Equations S3).

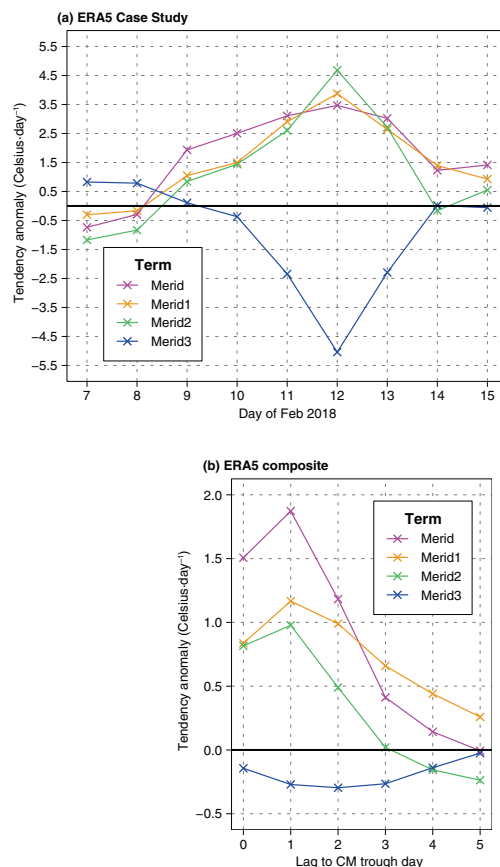


**FIGURE 12** ERA5 850-hPa meridional temperature advection (estimated from ERA5 day-mean 850-hPa fields) averaged over the ESL domain. (a) Meridional temperature advection anomalies during the case study. Full meridional term (Merid), and meridional terms Merid1, Merid2 and Merid3) (as described in the text and Equation S3b). The average is made applying the orography mask as shown on Figure S7 (gray shading) and values are rescaled to be for the anomaly relative to the 85-day mean based on February 2018–2020 (for comparison with YOPP results). (b) Same as (a) but for the mean composite anomaly for the 20% of strongest winter Central Mediterranean upper-level troughs (applying the methodology as in W21, therefore compositing a total of 946 troughs). Lag 0 is the advection composite averaged on the same day as the strong troughs, and Lags 1–5 shows the advection observed in the Days 1–5 following the day of strong trough. For the case study, 10 February is the day of strong Central Mediterranean trough, therefore for reference, Lag 0 on (b) may be compared with 10 February on (a), Lag 1 on (b) compared with 11 February on (a), etc. [Colour figure can be viewed at [wileyonlinelibrary.com](https://onlinelibrary.wiley.com/doi/10.1002/qj.70058)]

Over ESL, the full meridional advection during Days 3–5 (i.e., 10–12 February, see Figure 12a, Merid) is contributed to almost equally by the mean wind operating on the anomalous temperature gradient (Merid1) and the anomalous wind operating on the mean temperature gradient (Merid2). Based on Hu et al. (2019) we anticipated that Merid1 would grow to dominate as the event developed, but that does not happen here during Days 3–5.

Furthermore, by Day 4, and especially Day 5 (12 February) the anomalous wind operating on the anomalous temperature gradient (Merid3) serves as a strong damping on the event.

We suspected this evolution may be atypical, and to check this, undertook an analysis of the advection evolution following all strong CM troughs (top 20 percentile) during winters 1982–2020, applying the composite methodology in W21. Now (Figure 12b), the evolution supports the hypothesis of Hu et al. (2019), with Merid1 becoming the leading term 1 day after the CM trough (equivalent to Day 4, i.e., 11 February in the case study sequence) and indeed, Merid1 dominates onwards. The Merid3 term has a damping sense as in the case study, but very much weaker.

We hypothesize that the atypical behavior of the terms in the case study (Figure 12a) results partly from the approaching cold front, impacting the timing and detailed nature of the wind anomalies. Indeed, north of ESL, winds can briefly become weak actual southerlies as the front approaches, but without a long track of actual southerlies from the deep tropics. However, in addition to the approaching cold front, conditions to the south of ESL (Section 6.2) may also be influencing the atypical term behavior over ESL itself. Such details require further investigation in other ESL warm event settings. Nonetheless, a key conclusion here is that, averaged over all CM troughs, we do see the process proposed by Hu et al. (2019) operating to extend the longevity of the ESL warm event, here objectively calculated as term Merid1.

## 6.2 | Conditions to the south of ESL

Over ESL, there is a general transition from anomalous descent in the case study build-up, to anomalous ascent up to 650 hPa (averaged over Days 3–5) associated with anomalous Dyna(vert) cooling (Figure 10b). However, Day 3 is unique in its anomalous vertical motion signature, pausing the transition and actually displaying moderate anomalous low-level descent (Figures 13a and S8). A candidate to explain this pause in transition are the Day 3 anomalies just to the south of ESL (Figure 13a,b), extending southward into NEC where strong convective storms develop (Figure 2). Indeed, anomalous low-level warmth over ESL enhances the chances of such storm development (T18, W21), even though they are climatologically relatively rare in February, when rainfall is typically confined south of NEC. It turns out that for the case study sequence, this is the only day of strong NEC storms.

The composite low-level circulation associated with NEC high rain days at this time of year (W21) and in the event here (Figure 13a) shows anomalous southwesterly

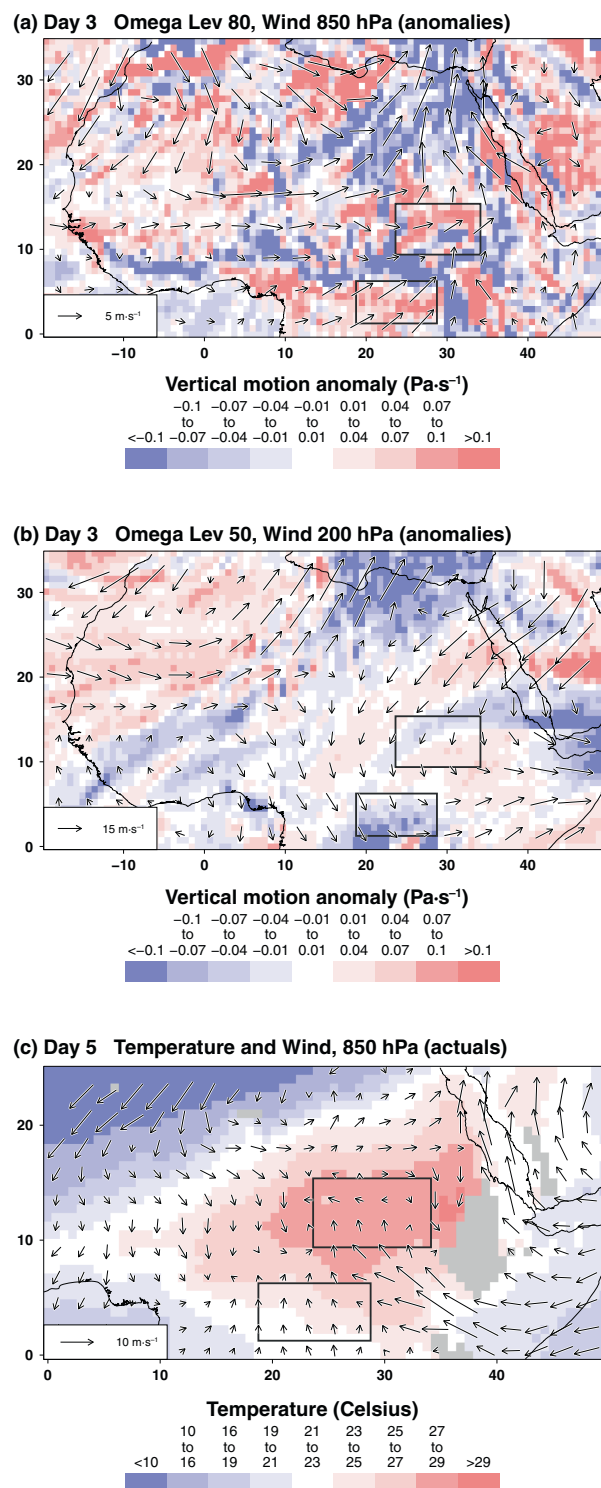


**FIGURE 13** (a) Day 3 (10 February 2018) YOPP day-mean forecast fields for anomalous vertical motion at model level 80 (approximately 850 hPa over ESL) along with anomalous 850-hPa wind. (b) Same as (a) but for model level 50 (approximately 210 hPa over ESL) and anomalous 200-hPa wind. (c) Same as (a) but for Day 5 (12 February 2018) actual 850-hPa fields of temperature and wind. Gray masking and wind vectors removed for areas below the surface (same procedures as Figure 4). [Colour figure can be viewed at [wileyonlinelibrary.com](https://onlinelibrary.wiley.com/doi/10.1002/qj.70058)]

extending through NEC, continuing and converging into a zone just south of ESL, interpreted to represent an anomalously northward migration of the ITD/heat low (HL) complex (Fink et al., 2011; W23), and showing on the satellite images over these latitudes with partially developed convection clouds (Figure 2). The major storms are further south (Figure 2), with vertical motion penetrating to upper levels (Figure 13b). Therefore, an avenue for future research is to consider whether the proximity to ESL of the NEC storms in conjunction with the even closer ITD/HL and strong anomalous rising motion through the boundary layer (Figure 13a) can systematically induce anomalous descent over ESL and the accompanying warming contribution from adiabatic compression. Nonetheless, such contribution during the case study is secondary in nature, and of much smaller magnitude compared to that from horizontal advection (Figure 10b).

The presence of strong anomalous low-level southerly wind anomalies near and north of ESL during Days 3–5 (Figures 4d,e, 13a) poses the question of whether low-level winds actually turn southerly and tap into air to the south of ESL from the deep tropics. In fact, over ESL, winds remain northerly throughout the case study Days 0–4, and only on Day 5, is there actual southerly flow that penetrates into southern parts of ESL (Figure 13c). By this time, the latitude of warmest low-level temperatures at these longitudes has migrated north to reside over ESL (Figure 13c), so it is considered that the collapse of northerly cold advection has been sufficient to allow this migration. This interpretation is supported by consulting the HL latitude calculations of W23 which, averaged over ESL longitudes, suggests HL migration from 6.4° N on Day 0 to 11.0° N on Day 5. On Day 5, the southerly flow entering southern parts of ESL is part of a strong push of southeasterlies from East Africa (Figure 13c) including through the Turkana Channel (Talib et al., 2023). Because the temperature maximum is now located over ESL, these winds cannot represent actual warm advection, however they can continue the anomalous warm advection and also can be expected to herald a change in weather type, representing a further research avenue to assess the details and frequency of this transition during ESL warm events.

## 7 | CONCLUDING DISCUSSION

A better understanding of the low-level northern Africa temperature changes following midlatitude winter troughs has been sought through focus on the temperature tendency mechanisms that operate. A case study was undertaken, containing the transition from a strong Iberia (IB) trough (Day 0) to strong Central Mediterranean (CM) trough (Day 3). The case study was selected as a strong

example of the repeating sequences composited in previous papers (W21, W23). While the case study has many features that suggest it is representative, it is important to caveat that the mechanisms identified now require verification across other events to appreciate the extent of their general applicability, and the details for ESL, need to be checked in other sub-regions.

At the regional scale, the low-level temperature tendency during this case study is primarily attributed to dynamics (Dyna), with the next most important tendency term being turbulent diffusion (Turb), that acts to partially damp Dyna. The strong IB trough initiates anomalous Dyna warming over central northern Africa that weakly extends to eastern parts, while anomalous Dyna cooling prevails near and behind the trough. When the IB trough transitions to CM trough, warm anomalies grow over the subsequent days over northeastern Africa. Days 3–5 mark the most pronounced extension of the warming southward into the eastern Sahel (ESL). For this case study, moisture anomalies are generally negative in the areas impacted by anomalous Dyna warming, such that anomalous radiation tendency in the boundary layer is generally negative (away from the surface) and therefore also acts as a damping agent, though with much less magnitude than Turb.

At this time of year, over ESL and much of northern Africa, the low-level Harmattan northerly is delivering cold advection. The wind anomalies associated with the CM trough (and more weakly, with the IB trough) dial down the northerly over northeastern Africa, leading to reduced cold advection. Anomalous low-level southerly winds prevail, but these do not represent actual southerly winds tapping into air from the deep tropics; rather the collapse of northerly cold advection is sufficient to lead to the substantial warming over northeastern Africa that in the case study even migrates the latitude of maximum low-level temperature northward into ESL. It is proposed that this specific weather sequence phenomenon, capable of delivering rapid swings of warming (and cooling), motivates more detailed human health impact perspectives.

The anomalous Dyna process is confined to low levels; over ESL to below 800 hPa. Above this level, climatological winds become light over ESL, quickly becoming predominantly westerly to the north, with very weak meridional component by 700 hPa over the broad northeastern Africa region, both in the climatology and in the anomalies for Days 3–5; hence there is no opportunity for meridional temperature advection anomalies.

During Days 3–5 over ESL, the afternoon BLH rises to near 650 hPa for several hours, when Turb shares some of the low-level anomalous warming from advection into the 800–650 hPa zone. This results in the net tendency anomaly remaining positive to near 650 hPa, though with diminishing magnitude.

Over ESL, Dyna has been separated into its contributions from horizontal motion (Dyna(hori), i.e., horizontal advection) and vertical motion (Dyna(vert)). During the core of the warm event over ESL (Days 3–5), generally anomalous rising motion occurs up to 650 hPa, and Dyna(vert) contributes a negative temperature tendency anomaly. From near-surface to 800 hPa, this represents a small damping on the anomalous Dyna(hori) warming. However, from 800 to 650 hPa, Dyna(vert) is the main Dyna tendency, and delivers a moderate damping to the Turb warming at these levels. Further work is needed to confirm if this is indicative of the boundary layer moving closer to the type identified in Parker et al. (2005) and Attwood et al. (2024) in the vicinity of summer West and southern Africa heat lows.

The land surface warms, but there is no suggestion of any anomalous source other than the anomalous warm advection in the lower boundary layer. The warming becomes shared with the land surface through interaction of the diurnal cycle with the anomalous warm advection, leading to the land surface warming especially fast in the morning hours. However, there is no evidence of any positive feedbacks, such as surface latent heating. A caveat concerns the use of model fields, and especially for the surface aspects, further validation using observations (beyond the surface temperature reported here for KH) will add further confidence to the interpretations. Nonetheless, the initial conditions of the YOPP forecasts draw on a variety of observational sources, and through this, the first hours of the forecasts are observationally constrained. A further aspect that builds confidence in the results is their consistency whether  $t + 0$  to  $t + 24$  or  $t + 24$  to  $t + 48$  segments of the forecasts are drawn upon.

Ahead of the case study days, there is a persistent strong IB trough (a feature also seen in W21). On these days, anomalous descent is generally found through the depth of the ESL troposphere, and Dyna(vert) contributes to a slow low-level warming tendency (Figure 10c). This motivates further investigation, including to assess if a strong persistent IB trough situation could amplify the impact of the subsequent CM trough on ESL. It is also found that NEC storms, which are more likely in the presence of ESL warmth (T18), are associated in the case study with distinct circulation signature over ESL. Also needing further consideration, is a possible role for intraseasonal tropical atmospheric modes (Guigma et al., 2021) in modulating the receptiveness of the Sahel to the winter trough impacts.

Based on previous work (Hu et al., 2019) it was anticipated that the longevity of the warm event over ESL might be attributed to the strong climatological northerlies operating on the anomalous temperature gradient (Merid1, Supporting Equations S3b). A composite over

all strong CM troughs does confirm this expectation (Figure 12b). However, for the case study Days 3–5, anomalous wind operating on climatological temperature gradient (Merid2) continues to be equally important, possibly related to the approaching cold front. Therefore, the case study has not had opportunity to study in detail days when the warm event is uniquely extended by Merid1. In such situations when circulation anomalies become weak, the way in which the anomalous temperature gradient is maintained, with a possible role for land surface persistence, needs to be considered.

Other examples of cold front engagement need to be studied to draw general conclusions on frequency of occurrence and typical impacts within the trough-induced warm event. Similar frontal activity has been noted in other sub-tropical semi-arid settings as well (e.g., Berry & Reeder, 2016). Substantial advances in Mediterranean cyclone knowledge in recent years (Flaounas et al., 2022; Hatzaki et al., 2023; Lionello et al., 2016) have mostly focused on the Mediterranean and impacts northwards; results here motivate extension to situations where a cold front develops and trails into northern Africa. Indeed, more generally, how the tropical circulation anomalies are excited by the midlatitude troughs warrants further investigation, and will likely involve recourse to Rossby wave propagation and type (e.g., De Vries et al., 2024; Knippertz, 2007).

In summary, the case study has highlighted multi-scale processes leading to weather anomalies at regional and sub-regional scales. Regional-scale upper-level winter troughs (Figure 3a,b), that likely relate to Rossby waves on the nearby midlatitude and subtropical waveguides (e.g., Röthlisberger et al., 2016; Knippertz, 2007; W23), develop expression in low-level wind and temperature anomaly fields over northern Africa reaching southward to near 5–10° N (Figures 3b,c, 4d,e). The key temperature driver is Dyna, mainly horizontal advection, in the low-to-mid boundary layer (Figures 5b–d, 10b), with widespread warming resulting over northeastern Africa (with similarities to Hu et al., 2019). Focusing at the sub-regional scale on ESL, the boundary-layer diurnal cycle is perturbed in the presence of the reduced cold advection. Boundary-layer height is much above normal in the afternoon hours (Figure 8a), and anomalous turbulent warming in the upper boundary-layer develops (Figures 7, 9a), drawing on the anomalously warm lower levels. The early hours of the day after sunrise is when near-surface warming tendency is most anomalous (Figures 9d, 11a,c), when accumulated overnight warm advection anomalies (Figure 9c) appear to be now shared towards the surface, and morning surface features become strongly perturbed (Figure 11a–d). By Day 5 of the case study, the latitude of maximum low-level heat



has migrated northward into ESL (Figure 13c), consistent with the anomalous boundary-layer characteristics (Fink et al., 2011; Parker et al., 2005). Further multiscale developments occur because the presence of the troughs can spawn Mediterranean cyclones (Figures 3a,b, S2e–h) which may (TP77), and indeed in this case did, develop a trailing cold front (Figures 3b,c, S2b–d) that brings smaller-scale focus to the resulting cold and warm advection anomalies, as well possible vertical motion cooling impacts, over northeastern Africa (Figures 5c–e, 6d, S4d).

To assess the extent to which ESL results are more widely applicable, the analyses now need repeating across other northern Africa domains and in association with winter troughs through the full eastern Atlantic–East Mediterranean belt that have all been shown to trigger several days of low-level warming extending to deep tropical latitudes (Knippertz & Fink, 2008; W23). This case study did not have a strong moisture plume or dust activity in the area of anomalous warm advection, both of which could potentially provide a feedback on the warming. In fact, as TP77 suggested, dust would be more likely in the presence of enhanced northerly cold advection at this time of year, with the anomalous warm advection typically associated with weakening of wind magnitude and therefore less chance of dust generation. In contrast, fronts in the transition seasons over northeastern Africa are often associated with desert cyclones (khamsin cyclones) and the khamsin weather type ahead of the associated front, with strong warm southerly winds that often entrain dust (e.g., TP77; Morales, 1980; Goudie, 1983; Al-Mutairi et al., 2023). This motivates consideration of the representation of dust in more detail in models like the IFS. However, in the absence of such features operating here, this case study has therefore illustrated how the driver of low-level horizontal advection anomalies has been able to generate a major low-level warm event, that extends into the surface and higher up to the afternoon levels of the boundary layer.

## ACKNOWLEDGEMENTS

The authors are grateful to the data providers: ERA5 data were provided by ECMWF via the Copernicus Climate Change Service (Hersbach et al., 2023). Neither the European Commission nor ECMWF is responsible for any use that may be made of the Copernicus information or data it contains. YOPP data were obtained through the ECMWF Public Datasets Service and can now be downloaded from the ECMWF MARS archive, see [www.ecmwf.int/en/forecasts/dataset/year-polar-prediction](http://www.ecmwf.int/en/forecasts/dataset/year-polar-prediction). This data is published under a Creative Commons Attribution 4.0 International (CC BY 4.0), see <https://creativecommons.org/licenses/by/4.0/>, Copyright “© European Centre for Medium-Range Weather Forecasts (ECMWF)”. ECMWF does not accept any liability whatsoever for any error


or omission in the data, their availability, or for any loss or damage arising from their use. Satellite images from MSG SEVIRI; surface observations from GSOD, served by OGIMET (<https://ogimet.com/gsodc.phtml.en>). Parker was supported by AMMA-2050, IMPALA (NER-C/DFID NE/M020126/1 and NE/M017176/1) and by UK Research and Innovation as part of the Global Challenges Research Fund, African SWIFT programme, grant number NE/P021077/1; RJK has been supported by CEMAC, University of Leeds. The second author acknowledges support by the Deutsche Forschungsgemeinschaft (grant no. SFB/TRR 165, “Waves to Weather”) and conducted within the subproject C2: “Statistical-dynamical forecasts of tropical rainfall”. The authors thank the three reviewers for their comments that led to numerous improvements in the manuscript.

## DATA AVAILABILITY STATEMENT

All data analyzed are archived by respective scientific institutions and are available to download. ERA5 data were provided by ECMWF via the Copernicus Climate Change Service (Hersbach et al., 2023). YOPP data were obtained through the ECMWF Public Datasets Service and can now be downloaded from the ECMWF MARS archive, see [www.ecmwf.int/en/forecasts/dataset/year-polar-prediction](http://www.ecmwf.int/en/forecasts/dataset/year-polar-prediction). The surface weather station observations that are used are available through WMO-GSOD, served by OGIMET <https://ogimet.com/gsodc.phtml.en>. The satellite images used are available from MSG SEVIRI <https://user.eumetsat.int/data-access>.

## ORCID

Neil Ward  <https://orcid.org/0000-0003-1385-0349>

Andreas H. Fink  <https://orcid.org/0000-0002-5840-2120>

Douglas J. Parker  <https://orcid.org/0000-0003-2335-8198>

## REFERENCES

- Al-Mutairi, M., Labban, A., Abdeldym, A., Alkhouly, A., Abdel Bas-set, H. & Morsy, M. (2023) Diagnostic study of a severe dust storm over North Africa and the Arabian peninsula. *Atmosphere*, 14(2), 196.
- Andrews, P.C., Cook, K.H. & Vizi, E.K. (2024) Mesoscale convective systems in The Congo Basin: seasonality, regionality, and diurnal cycles. *Climate Dynamics*, 62(1), 609–630.
- Attwood, K., Washington, R. & Munday, C. (2024) The southern African heat low: structure, seasonal and diurnal variability, and climatological trends. *Journal of Climate*, 37(10), 3037–3053.
- Bauer, P., Sandu, I., Magnusson, L., Mladek, R. & Fuentes, M. (2020) ECMWF global coupled atmosphere, ocean and sea-ice dataset for the year of polar prediction 2017–2020. *Scientific Data*, 7(1), 427.
- Berry, G.J. & Reeder, M.J. (2016) The dynamics of Australian monsoon bursts. *Journal of the Atmospheric Sciences*, 73(1), 55–69.

- Carlson, T.N. (1994) *Mid-latitude weather systems*. New York: Routledge, p. 507.
- Cook, K.H. & Vizzy, E.K. (2015) Detection and analysis of an amplified warming of the Sahara Desert. *Journal of Climate*, 28(16), 6560–6580.
- Cook, K.H. & Vizzy, E.K. (2024) Understanding the regionality and diurnal cycles of precipitation in the Lake Victoria Basin during boreal fall. *Climate Dynamics*, 62(2), 1359–1378.
- Cook, K.H., Liu, Y. & Vizzy, E.K. (2020) Congo Basin drying associated with poleward shifts of the African thermal lows. *Climate Dynamics*, 54(1), 863–883.
- De Vries, A.J., Armon, M., Klingmüller, K., Portmann, R., Röthlisberger, M. & Domeisen, D.I. (2024) Breaking Rossby waves drive extreme precipitation in the world's arid regions. *Communications Earth & Environment*, 5(1), 493.
- Fink, A.H., Agustí-Panareda, A., Parker, D.J., Lafore, J.P., Ngamini, J.B., Afiesimama, E. et al. (2011) Operational meteorology in West Africa: observational networks, weather analysis and forecasting. *Atmospheric Science Letters*, 12(1), 135–141.
- Fink, A.H., Engel, T., Ermert, V., Van Der Linden, R., Schneidewind, M., Redl, R. et al. (2017) Mean climate and seasonal cycle. In: Parker, D.J. & Diop-Kane, M. (Eds.) *Meteorology of tropical West Africa: the forecasters' handbook*. Hoboken, NJ: Wiley, pp. 1–39.
- Flaounas, E., Davolio, S., Raveh-Rubin, S., Pantillon, F., Miglietta, M.M., Gaertner, M.A. et al. (2022) Mediterranean cyclones: current knowledge and open questions on dynamics, prediction, climatology and impacts. *Weather and Climate Dynamics*, 3(1), 173–208.
- Fontaine, B., Janicot, S. & Monerie, P.A. (2013) Recent changes in air temperature, heat waves occurrences, and atmospheric circulation in northern Africa. *Journal of Geophysical Research: Atmospheres*, 118(15), 8536–8552.
- Garcia-Carreras, L., Parker, D.J., Marsham, J.H., Rosenberg, P.D., Brooks, I.M., Lock, A.P. et al. (2015) The turbulent structure and diurnal growth of the Saharan atmospheric boundary layer. *Journal of the Atmospheric Sciences*, 72(2), 693–713.
- Goudie, A.S. (1983) Dust storms in space and time. *Progress in Physical Geography: Earth and Environment*, 7(4), 502–530.
- Guigma, K.H., Guichard, F., Todd, M., Peyrille, P. & Wang, Y. (2021) Atmospheric tropical modes are important drivers of Sahelian springtime heatwaves. *Climate Dynamics*, 56(5), 1967–1987.
- Hart, N.C.G., Washington, R. & Maidment, R.I. (2019) Deep convection over Africa: annual cycle, ENSO, and trends in the hotspots. *Journal of Climate*, 32(24), 8791–8811.
- Hatzaki, M., Flaounas, E., Davolio, S., Pantillon, F., Patlakas, P., Raveh-Rubin, S. et al. (2023) MedCyclones: working together toward understanding Mediterranean cyclones. *Bulletin of the American Meteorological Society*, 104(2), E480–E487.
- Hersbach, H., Bell, B., Berrisford, P., Biavati, G., Horányi, A., Muñoz Sabater, J. et al. (2023) ERA5 hourly data on pressure levels from 1940 to present. *Copernicus Climate Change Service (C3S) Climate Data Store (CDS)*. Available from: <https://doi.org/10.24381/cds.bd0915c6>
- Hersbach, H., Bell, B., Berrisford, P., Hirahara, S., Horányi, A., Muñoz-Sabater, J. et al. (2020) The ERA5 global reanalysis. *Quarterly Journal of the Royal Meteorological Society*, 146(730), 1999–2049.
- Hu, L., Luo, J.J., Huang, G. & Wheeler, M.C. (2019) Synoptic features responsible for heat waves in Central Africa, a region with strong multidecadal trends. *Journal of Climate*, 32(22), 7951–7970.
- Jung, T., Wilson, J., Bazile, E., Bromwich, D., Casati, B., Day, J. et al. (2025) The year of polar prediction (YOPP): achievements, impacts and lessons learnt. *Bulletin of the American Meteorological Society*. Available from: <https://doi.org/10.1175/BAMS-D-23-0226.1>
- Knippertz, P. (2004) A simple identification scheme for upper-level troughs and its application to winter precipitation variability in Northwest Africa. *Journal of Climate*, 17(6), 1411–1418.
- Knippertz, P. (2007) Tropical–extratropical interactions related to upper-level troughs at low latitudes. *Dynamics of Atmospheres and Oceans*, 43(1–2), 36–62.
- Knippertz, P. & Fink, A.H. (2008) Dry-season precipitation in tropical West Africa and its relation to forcing from the extratropics. *Monthly Weather Review*, 136(9), 3579–3596.
- Laing, A., Hamidou, H., Diop-Kane, M. & Wardle, T. (2017) Remote sensing. In: Parker, D.J. & Diop-Kane, M. (Eds.) *Meteorology of tropical West Africa: the forecasters' handbook*. Hoboken, NJ: Wiley, pp. 323–379.
- Largerion, Y., Guichard, F., Roehrig, R., Couvreux, F. & Barbier, J. (2020) The April 2010 north African heatwave: when the water vapor greenhouse effect drives nighttime temperatures. *Climate Dynamics*, 54(9), 3879–3905.
- Lavaysse, C., Flamant, C., Janicot, S., Parker, D.J., Lafore, J.-P., Sultan, B. et al. (2009) Seasonal evolution of the west African heat low: a climatological perspective. *Climate Dynamics*, 33(2), 313–330.
- Lionello, P., Trigo, I.F., Gil, V., Liberato, M.L., Nissen, K.M., Pinto, J.G. et al. (2016) Objective climatology of cyclones in the Mediterranean region: a consensus view among methods with different system identification and tracking criteria. *Tellus A: Dynamic Meteorology and Oceanography*, 68(1), 29391.
- Morales, H.C. (1980) A case study of a dust storm weather situation in The Sudan in April 1973. *Pure and Applied Geophysics*, 119(3), 658–676.
- NASA. (2024) March 2024 Sudan Heat Wave Through GEOS-S2S-2. <https://gmao.gsfc.nasa.gov/science-snapshots/march-2024-sudan-heat-wave-through-geos-s2s-2/>.
- NOAA National Centers of Environmental Information. (1999) Global Surface Summary of the Day - GSOD. 1.0., as served through OGIMET. <https://ogimet.com/gsocd.phtml.en>.
- Oke, T.R. (1987) *Boundary layer climates*, 2nd edition. New York: Routledge, p. 435.
- Oueslati, B., Pohl, B., Moron, V., Rome, S. & Janicot, S. (2017) Characterization of heat waves in the Sahel and associated physical mechanisms. *Journal of Climate*, 30(9), 3095–3115.
- Parker, D.J., Burton, R.R., Diongue-Niang, A., Ellis, R.J., Felton, M., Taylor, C.M. et al. (2005) The diurnal cycle of the west African monsoon circulation. *Quarterly Journal of the Royal Meteorological Society*, 131(611), 2839–2860.
- Ragatoa, D.S., Amekudzi, L.K., Fink, A.H., Maranan, M., Klutse, N.A.B., Edjame, K.S. et al. (2024) Droughts and heatwaves in the west African monsoon system. *International Journal of Climatology*, 44(11), 3681–3705.
- Rasheeda Satheesh, A., Knippertz, P. & Fink, A.H. (2025) Machine learning models for daily rainfall forecasting in northern tropical Africa using tropical wave predictors. *Weather and Forecasting*, 40(10), 1895–1916.
- Röthlisberger, M., Martius, O. & Wernli, H. (2016) An algorithm for identifying the initiation of synoptic-scale Rossby waves on

- potential vorticity waveguides. *Quarterly Journal of the Royal Meteorological Society*, 142(695), 889–900.
- Talib, J., Taylor, C.M., Harris, B.L. & Wainwright, C.M. (2023) Surface-driven amplification of Madden–Julian oscillation circulation anomalies across East Africa and its influence on the Turkana jet. *Quarterly Journal of the Royal Meteorological Society*, 149(754), 1890–1912.
- Taylor, C.M., Fink, A.H., Klein, C., Parker, D.J., Guichard, F., Harris, P.P. et al. (2018) Earlier seasonal onset of intense mesoscale convective systems in The Congo Basin since 1999. *Geophysical Research Letters*, 45(24), 13458–13467.
- Tucker, M.R. & Pedgley, D.E. (1977) Synoptic disturbances over the Nile valley north of the intertropical convergence zone. *Tellus*, 29(1), 17–24.
- Varga, G. (2020) Changing nature of Saharan dust deposition in the Carpathian Basin (Central Europe): 40 years of identified north African dust events (1979–2018). *Environment International*, 139, 105712.
- Vizy, E.K. & Cook, K.H. (2014) Impact of cold air surges on rainfall variability in the Sahel and wet African tropics: a multi-scale analysis. *Climate Dynamics*, 43(3), 1057–1081.
- Ward, N., Fink, A.H., Keane, R.J. & Parker, D.J. (2023) Upper-level midlatitude troughs in boreal winter have an amplified low-latitude linkage over Africa. *Atmospheric Science Letters*, 24(1), e1129.
- Ward, N., Fink, A.H., Keane, R.J., Guichard, F., Marsham, J.H., Parker, D.J. et al. (2021) Synoptic timescale linkage between midlatitude winter troughs Sahara temperature patterns and northern Congo rainfall: a building block of regional climate variability. *International Journal of Climatology*, 41(5), 3153–3173.

## SUPPORTING INFORMATION

Additional supporting information can be found online in the Supporting Information section at the end of this article.

**How to cite this article:** Ward, N., Fink, A.H., Keane, R.J. & Parker, D.J. (2025) A case study of temperature tendency mechanisms operating over northern Africa during and following midlatitude winter troughs. *Quarterly Journal of the Royal Meteorological Society*, e70058. Available from: <https://doi.org/10.1002/qj.70058>